https://doi.org/10.5194/egusphere-2024-3289
Preprint. Discussion started: 4 November 2024

Wind and wave effects on the dispersal of the Pearl River-derived sediment over the Shelf

Guang Zhang[1,2,3], Suan Hu[1,2,3], Xiaolong Yu[1,2,3], Heng Zhang[1,2,3], Wenping Gong[1,2,3]*

[1] School of Marine Sciences, Sun Yat-sen University, Guangzhou, China, 510275

[2] Guangdong Provincial Key Laboratory of Marine Resources and Coastal Engineering, Guangzhou 510275, China

[3] Pearl River Estuary Marine Ecosystem Research Station, Ministry of Education, Zhuhai 519082, China

Corresponding author: Wenping Gong (gongwp@mail.sysu.edu.cn)

https://doi.org/10.5194/egusphere-2024-3289
Preprint. Discussion started: 4 November 2024

Abstract

The transport processes of suspended sediment from river sources to ocean sinks are vital for the global material cycle. This study quantitatively examines the effects of wind and wave dynamics on riverine sediment transport over a continental shelf throughout a typical year, utilizing the Coupled Ocean Atmosphere Wave Sediment Transport (COAWST) model. After meticulous calibration, the model effectively replicates various fundamental marine environmental processes. Key findings reveal that over a typical year, approximately 62% of riverine sediment is retained near the estuary, with sediments primarily transported southwestward and deposited in Beibu Gulf. During the wet summer, calm winds and waves lead to initial sediment deposition near the estuary via the river plume. In contrast, the dry winter sees stronger winds and waves resuspending and transporting these sediments. Analyses demonstrate that combined wind and wave action reduces proximal riverine sediment deposition levels to 83% of those under No wind or wave conditions, resulting in a fivefold increase in westward alongshore sediment flux. Additionally, intensified cross-shore gradients of water level and density boost westward geostrophic flow and thermal wind shear, facilitating sediment transport to distant regions. This study offers valuable insights into the intricate interplay between winds, waves, and riverine sediment dynamics on continental shelves.

Keywords

Riverine sediment transport; Wind and wave; Sediment dynamics; Numerical modeling; Pearl River Estuary

https://doi.org/10.5194/egusphere-2024-3289
Preprint. Discussion started: 4 November 2024

1. Introduction

The transport process of suspended sediment from river source to ocean sink is an important link in the global material cycle (Cao et al., 2019;Kuehl et al., 2016;Liu et al., 2016). Much of the riverine sediment is trapped on the shallow shoals in estuaries, while the rest is transported by river plume out of the estuary (Burchard et al., 2018;Zhang et al., 2019;Meade, 1969). The riverine sediment carried by the river plume has a significant impact on the water quality, ecology, and geomorphology of the estuaries and continental shelves (Wright and Coleman, 1973;Turner and Millward, 2002).

The extent, transport pathway, and depocenter of riverine sediment on the continental shelf initially depend on the supply of sediments by the river plume (Wright and Nittrouer, 1995). Then, the ultimate dispersal and fate of the plume and riverine sediment are influenced by coastal currents, tides, winds, and waves (Dyer, 1997;Bever et al., 2009;Harris et al., 2008;Horner-Devine et al., 2015;Rong et al., 2014;Geyer et al., 2004). Winds and waves play a crucial role in shaping river plumes (Rong et al., 2014;Chi and Rong, 2023;Lai et al., 2016), estuarine and coastal circulation (Li and Li, 2011;Gan et al., 2013;Gan et al., 2009), and then influence the sediment resuspension, transport, and deposition in coastal and marine environments (Bever et al., 2009;Harris et al., 2008;Geyer et al., 2004).

Here, we use China's Pearl River Estuary (PRE) as a case study. The Pearl River ranks as China's second-largest river in terms of river discharge (Hu et al., 2011). The average annual (2001-2022) freshwater and riverine sediment loads are 2.74×10^{11} m^3

and 2.84×10^7 tons, as reported by the Ministry of Water Resources of the People's Republic of China (http://www.mwr.gov.cn/sj/#tjgb). Previous studies have investigated the total suspended sediment concentration (SSC) and its transport under impacts of typhoon or winter storm-induced wave-current effect in the PRE (Zhang et al., 2021;Liu and Cai, 2019;Yang et al., 2022). Outside the PRE, gravity core and seismic survey data were used to examine the Holocene sedimentary processes, revealing one proximal and one distal mud belt extending southeastward and southwestward, respectively (Ge et al., 2014;Chen et al., 2023;Liu et al., 2014).

However, seismic and drilling data cannot confirm that the Pearl River sediment can be transported to the Beibu Gulf (Ge et al., 2014). Due to the lack of sufficient gravity core samples and seismic data, it is difficult to quantitatively attribute the sediment in the Beibu Gulf to the Pearl River-derived sediment (Cao et al., 2019). Afterward, Lin et al. (2020) used the ^{226}Ra—^{238}U and ^{232}Th—^{238}U endmembers model based on measurements of radionuclides in surface sediment samples. They found that approximately 15% of the surface sediment in the nearshore area of the Beibu Gulf originates from the PRE region. However, their studies only address the proportion of PRE sediment in the surface sediment of the Beibu Gulf, without directly indicating the transport pathways, flux, and mechanisms of sediment from the Pearl River.

Therefore, the specific processes of sediment transport and deposition and the fate of the Pearl River-derived sediment on the continental shelf have not been adequately addressed. Although several studies have delved into the Pearl River-derived sediment suspension, transport, and budgets within the PRE (Zhang et al., 2019;Hu et al., 2011;Xia et al., 2004), research on riverine sediment dispersal beyond the estuary remains relatively limited. A gap persists in understanding how winds and waves influence the suspension, transport, and deposition of Pearl River-derived sediment on the shelf, including how it enters the Beibu Gulf.

This study focused on the processes of Pearl River-derived sediment suspension, transport, and deposition driven by winds and waves over the continental shelf. Several specific questions addressed in this paper include:

(1) What are the seasonal and annual patterns of the Pearl River sediment suspension, transport, and deposition over the continental shelf?

(2) How do the winds and waves affect the continental shelf hydrodynamics, subsequently influencing the transport and fate of the Pearl River sediment?

2. Study Region

The South China Sea, situated in the southern part of mainland China, is the largest marginal sea in the northwest Pacific (Figure 1a), covering approximately 3.5 million km^2, featuring a wide continental shelf in the northern part and adjoining the PRE (Zhong et al., 2017;Liu et al., 2014). The dynamic forcing of the sea surface exhibits significant seasonal variations: during summer, the prevailing southwest monsoon, with an average wind speed of 6 m s^{-1}, dominates the entire sea area, whereas the northeast monsoon, with an average wind speed of 9 m s^{-1}, prevails during winter (Su, 2004;Liu et al., 2014). Northeast-oriented shelf flow prevails in summer, contrasting with southwestward flow in winter, accompanied by distinct upwelling in summer and downwelling in winter, reflecting clear patterns of cross-shelf water exchange dynamics (Gan et al., 2009;Gan et al., 2013).

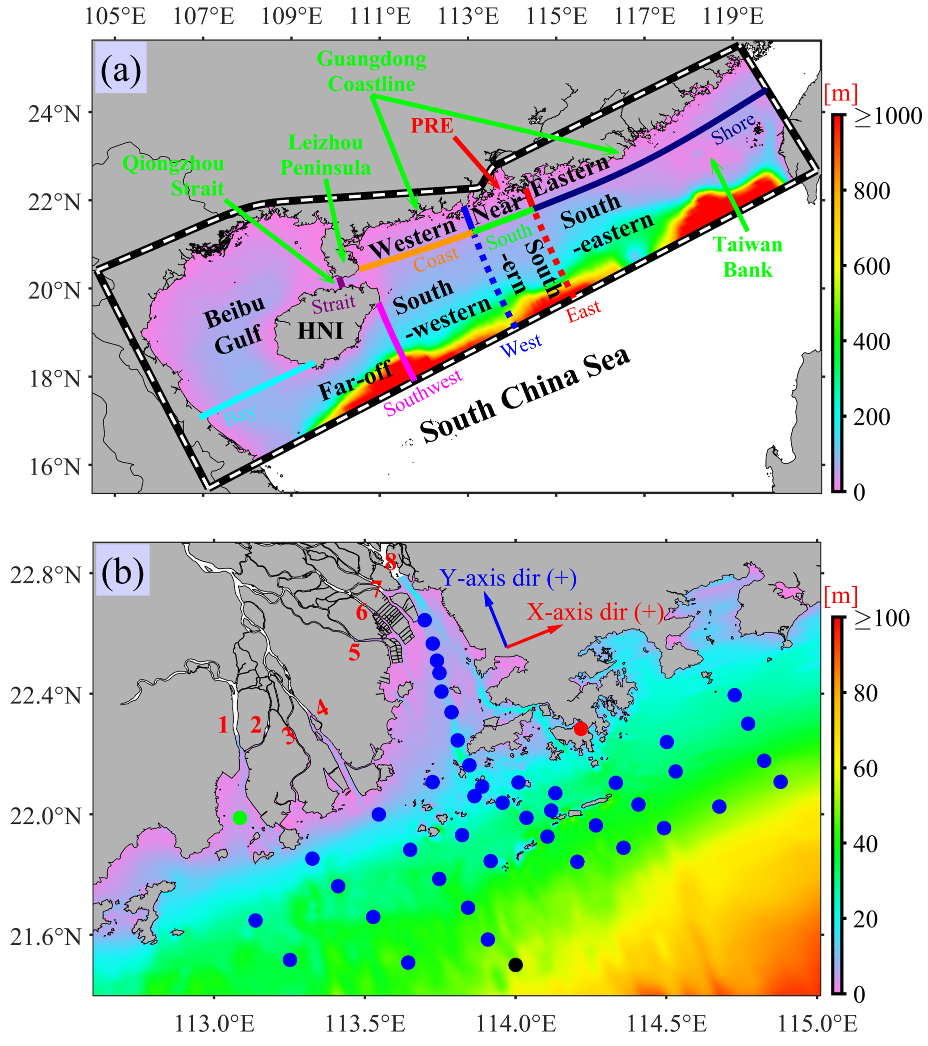

Figure 1. (a) Bathymetry (shading) and transects (same color as their respective names) on the model grid. (b) zoom in on the Pearl River Estuary (PRE) and nearby waters. The abbreviations HNI and PRE, mean Hainan Island and PRE, respectively. The observation stations, represented by red, green, blue, and black dots respectively, denote the Quarry Bay water level station, the 113-hour fixed onboard S1 station in

the PRE, 43 CTD stations during the voyage campaign, and wave station W. The red numbers 1-8 represent the eight outlets of the PRE, where Pearl River freshwater and sediment (the fourth and fifth sizes of sediments in Table 1 below) are discharged into the PRE. The X-axis and Y-axis represent the alongshore and cross-shore directions, respectively, as described in the main text and subsequent figures. The arrows indicate the positive direction of each axis.

The Pearl River experiences significant seasonal variations in freshwater and sediment discharges, with approximately 80% of freshwater and 95% of sediment load being discharged during the wet summer season from April to September (Xia et al., 2004). The Pearl River forms the complex PRE downstream, with freshwater and riverine sediments typically entering the PRE from eight outlets (Figure 1b; Wu et al., 2016;Zhang et al., 2019).

The PRE has a micro-tidal and mixed semi-diurnal regime, with daily inequality in the range and in the time between the high and low tides (Mao et al., 2004). The neap and spring tides alternately influence the water elevation downstream of the estuary, with tidal ranges varying from approximately 0.7 m during neap tides to approximately 2 m during spring tides (Gong et al., 2018;Chen et al., 2016). The PRE and the nearby shelf exhibit strong seasonal variation and are highly stratified during the wet summer season, while the PRE becomes partially mixed or vertically well-mixed during the dry winter season (Dong et al., 2004).

3. Methods

3.1 Model coupling

This study employed the Coupled Ocean Atmosphere Wave Sediment Transport (COAWST, version 3.4) modeling system (Warner et al., 2010;Warner et al., 2005;Warner et al., 2008), which includes a Model Coupling Toolkit to facilitate data exchange among different modules. The system mainly comprises a hydrodynamic module (Regional Ocean Modeling System; ROMS), an atmospheric module (Advanced Research Weather Research and Forecasting; WRF), a wave module (Simulating Waves Nearshore; SWAN), and a sediment transport module (Community Sediment Transport Modeling System; CSTM).

In this study, we established a coupling between ROMS, SWAN, and CSTM. The model grid covers the northern continental shelf of the South China Sea, including the PRE (Figure 1). The regional model was configured with 170×482 horizontal grid cells, with horizontal resolution varying from approximately 0.1 km near the PRE to about 10 km at outer open boundaries. The model grid bathymetry data was obtained from the Global Earth Bathymetry Data Set (GEBCO) and nautical charts compiled by the China Maritime Safety Administration. The vertical grid used a Sigma coordinate system with 20 layers and a stretching transformation for higher resolution near the surface and bottom, with stretching parameters of θ_s=3.0 and θ_b=3.0, respectively (Song and Haidvogel, 1994). For model validations, please refer to the Supplement file (Supplement Figures S1-S3).

3.2 ROMS model setup

For the ROMS models, we utilized the Generic Length Scale turbulence closure scheme (Warner et al., 2005) for vertical turbulence parameterization. The method of Smagorinsky (1963) was employed to calculate the horizontal eddy viscosity and diffusivity. The Flather and Chapman boundary conditions were applied to barotropic current and water elevation at open boundaries, respectively (Chapman, 1985;Flather, 1976). Meanwhile, the open-boundary conditions for temperature, salinity, and sediment concentration were imposed by radiation methods (Orlanski, 1976;Raymond and Kuo, 1984). Surface forcing (including wind, net shortwave radiation, air temperature, atmospheric pressure, specific/relative humidity, and rain, etc.) data were sourced from the Climate Forecast System Reanalysis of the National Centers for Environmental Prediction, with a temporal resolution of 1 h and a spatial resolution of 0.3° × 0.3°. Water level and current open-boundary conditions comprised two components: tidal and subtidal. The tidal component was obtained from the Oregon State University Tidal Prediction Software database (Egbert and Erofeeva, 2002), while the subtidal component was interpolated from the HYbrid Coordinate Ocean Model (HYCOM) outputs.

3.3 Wave model setup

The SWAN model was executed and coupled to the same grid as the ROMS model (Warner et al., 2010). It was driven by surface atmospheric forces, real-time water level, and current fields from the ROMS and boundary reanalysis data. Wave boundary conditions were specified using nonstationary wave parameters from outputs of the WAVEWATCH III model. Information exchange between the ROMS and SWAN models occurred at 15-minute intervals to introduce wave-current interaction (WCI). This exchange included significant wave height (Hsig), surface peak wave period, mean wave direction and length, wave energy dissipation, and the percentage of breaking waves from SWAN to ROMS, as well as water level and current from ROMS to SWAN.

3.4 Specifications of riverine input and sediment model

The freshwater discharge was specified at the northern boundary using daily measured data, while downstream precipitation was neglected. The full simulation model was initialized on the first day of January 2016 using temperature, salinity, and current fields interpolated from the HYCOM model, and it concluded on March 31, 2018. More than one year of hydrodynamic and sediment spin-up is sufficient to achieve appropriate seabed sediment particle size distribution, as well as stable circulation and thermohaline fields. This study primarily analyzes the last 12 months, specifically from April 1, 2017, to March 31, 2018. This year is selected because the freshwater discharge and sediment load of the Pearl River closely approximate the average values of the past two decades, with a runoff of 3.35×10^{11} m^3 and a sediment load of 3.45×10^7 tons, closely resembling the averages from 2001 to 2022.

Since the daily riverine sediment loads were unavailable, following previous research results on sediment rating curves (Zhang et al., 2012), the riverine sediment input calculated from the river discharge was specified at the eight outlets located on the north boundary (Figure 1b), between April 1, 2017, and March 31, 2018.

The subsequent step involves establishing the proportion of seabed sediment particle size components. Sediments are typically categorized into three grain-size classes: clay (0-4 μm), silt (4-63 μm), and sand (63-2000 μm), as outlined by Shepard (1954). Data on sediment particle size composition for the northern continental shelf of the South China Sea and the PRE area were acquired through multiple voyage observations (Zhang et al., 2013;Zhang et al., 2019). Furthermore, publicly available data from published literature were compiled (Gao et al., 2010;Gao et al., 2007;Ge et al., 2019;Ge et al., 2017;Huang et al., 2013;Kirby et al., 2008;Liu et al., 2014;Lu et al., 2017;Wang et al., 2016;Wang et al., 2015;Wang et al., 2014;Yang et al., 2018;Zhong et al., 2017). Finally, component distribution data for different particle size classes of seabed sediment were obtained from a total of 1981 measured stations (Figure 2a-c).

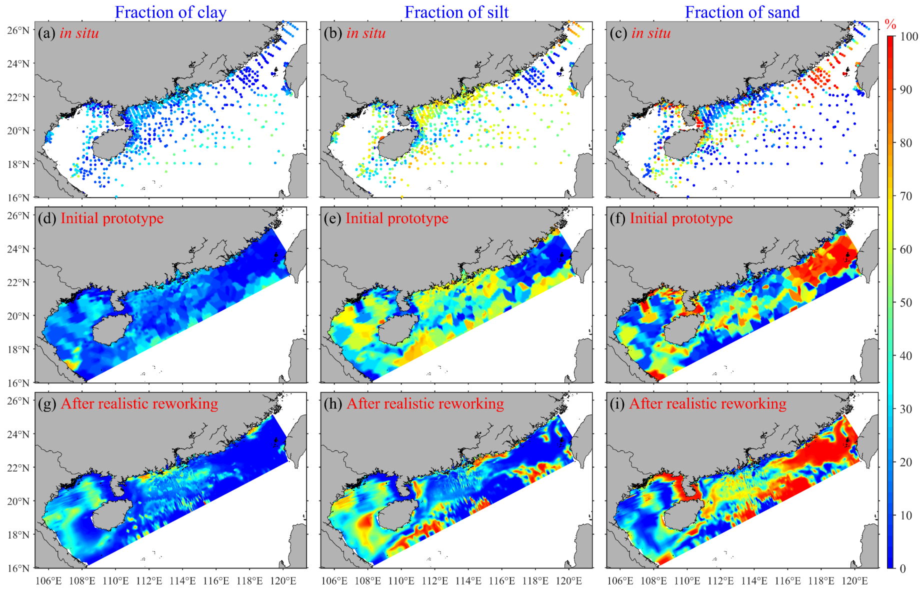

Figure 2. Row 1 illustrates the seabed spatial fractions observed across 1981 sites, while Row 2 exhibits the initial prototype of seabed spatial fractions distributions based on the observed data in Row 1. Row 3 showcases seabed spatial fractions distributions resulting from the model simulation on April 1st, 2017, with columns 1,

2, and 3 representing the fractions of clay, silt, and sand, respectively.

As illustrated in Figure 2a-c, the measured stations exhibit a widespread distribution, offering comprehensive coverage of the entire northern continental shelf of the South China Sea, including the PRE. Particularly dense distribution is observed in the PRE and the coastal areas of western Guangdong. These regions represent the primary scope of sediment transport and deposition associated with the Pearl River. Hence, the stations utilized in this study well represent the distribution of bed sediment particle size components in the study area. It is evident that among the stations in the offshore area of the northern continental shelf of the South China Sea, silt dominates, followed by clay, while sand with the largest particle size is the least abundant. This suggests a significant presence of terrestrial sediment or Pearl River sediment in the offshore area of the northern continental shelf of the South China Sea.

To derive the component proportions of the initial prototype field on the model grid, this study employed the Kriging method (Krige, 1951), widely recognized for spatially interpolating various types of observational data. The sediment distribution pattern obtained through interpolation (Figure 2d-f) closely resembles the original 1981 measured sediment particle size distribution patterns (Figure 2a-c), suggesting the suitability of this interpolation method for the study area.

The initial prototype field underwent a 15-month spin-up period (from January 1, 2016, to March 31, 2017), during which it was adjusted by realistic reworking, incorporating realistic winds in ROMS and SWAN models. This adjustment allowed for the redistribution of seabed sediment based on the modeled hydrodynamics. This method has been utilized in numerous previous studies, including those by Bever et al. (2009), van der Wegen et al. (2010), and Zhang et al. (2021). The realistic spin-up greatly reduced the irregularities and prepared a more suitable seabed sediment particle size distribution field for subsequent simulations than the initial prototype (Figure 2g-i).

During the simulations following spin-up, the CSTM utilized five sediment classes, including three types of seabed sediments (clay, silt, and sand, corresponding to the first three categories of sediments in Table 1) and two types of riverine suspended sediment from the Pearl River (the sum of the fourth and fifth sizes of sediments in Table 1, namely "Clay (river)" and "Silt (river)"). The parameters for all five sediment classes are summarized in Table 1. Here, we define the Pearl River sediment as the last two types of the specified sediment classes. Specifically, the fractions of clay and silt from the Pearl River were set at 40% and 60%, respectively, following Zhang et al. (2019) and Zhang et al. (2021). This approach allows for a better distinction between Pearl River sediment and seabed sediment, enabling separate analysis of the suspension, transport, and deposition of Pearl River sediment (Harris et al., 2008;Zhang et al., 2019). The settling velocity, critical shear stresses, and other parameters were set following previous studies or were based on model calibration (Zhang et al., 2019;Zhang et al., 2021;Ralston et al., 2012;Warner et al., 2017). To clarify, the following analysis does not include riverine sediment during the spin-up time, as this sediment was already classified as seabed sediment categories (clay and silt) by the beginning of the analysis in April 2017.

Table 1. CSTM model Sediment Properties

Sediment Class	Clay (bed)	Silt (bed)	Sand (bed)	Clay (river)	Silt (river)
Grain size (μm)	4	32	500[d]	1.84[ab]	11.7[ab]
Settling velocity (mm s^{-1})	0.02[e]	1.2[c]	57[d]	0.005[e]	0.6[c]
Critical stresses (Pa)	0.14[c]	0.03[c]	0.27[d]	0.15[ab]	0.05[abc]
Fraction	Spatially variable, see Figure 2g-i			40%[ab]	60%[ab]
Erosion rate (kg m^{-2} s^{-1})[c]	1×10^{-4}	1×10^{-4}	1×10^{-4}	1×10^{-4}	1×10^{-4}
Bottom porosity[ab]	0.672	0.672	0.672	0.672	0.672

[a]Zhang et al. (2019), [b]Zhang et al. (2021), [c]Ralston et al. (2012), [d]Warner et al. (2017), [e]Calibrated.

3.5 Wet and dry season regimes

Seasonal variations in the study area are pronounced and can be broadly classified into two distinct seasons. Various indicators such as river freshwater discharge, riverine sediment load (Figure 3a), wind patterns (Figure 3b), air temperature (Figure 3c), and wave conditions (Figure 3d-f) at the representative site (21.5°N, 114°E, just below the PRE) are utilized to characterize these seasons (Figure 3). The entire year (from April 1, 2017, to March 31, 2018) is typically divided into two main seasons: wet summer (from April 1, 2017, to September 30, 2017) and dry winter (from October 1, 2017, to March 31, 2018).

During the wet summer season, freshwater discharge tends to be notably high, often exceeding 10,000 m^3 s^{-1} and reaching a maximum of 53,000 m^3 s^{-1}, with an average value of 15,266 m^3 s^{-1}. This discharge constitutes a significant portion of the entire year, accounting for 72.06% of the annual total. Additionally, the riverine sediment load during this period is substantial, totaling 32.83 megatons, which represents 95.1% of the total annual amount. Prevailing winds predominantly blow from the south. For example, Figure 3b depicts the average monthly wind vector direction during the summer months as northward, with weak southeasterly winds in April, May, and September, and moderate southeasterly winds in July. June and August experience moderate southwesterly winds. The 2 m height air temperatures typically range between 20℃ and 30℃. The daily average Hsig remains relatively low, with the monthly average Hsig less than 1 m. The wave propagation direction is generally consistent with the wind direction, being easterly in April and May, and southerly from June to September.

In stark contrast, the dry winter season demonstrates markedly lower runoff, typically falling below 10,000 $m^3 s^{-1}$, with an average value of 5,953 $m^3 s^{-1}$. The sediment load during this period is merely 1.69 megatons, representing a significant decrease compared to the wet summer season. Prevailing winds during the dry winter are predominantly northeasterly, with relatively high wind speeds. Except for moderate wind intensity in March, the monthly average wind speed in other months exceeds 5 $m s^{-1}$. The 2 m height air temperatures typically range between 10℃ and 25℃ during this season. The wave propagation direction aligns with the prevailing northeasterly winds of the season, predominantly northeastly.

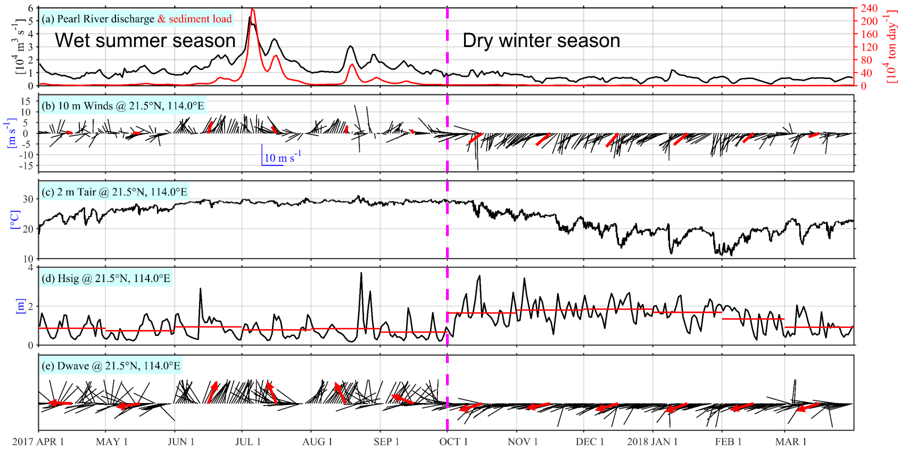

Figure 3. Time series of (a) the daily Pearl River freshwater discharge and sediment load, (b) daily (black vectors) and monthly (red vectors) averaged 10-meter height winds, (c) hourly 2-meter height air temperature, daily (black) and monthly (red) averaged (d) significant wave height (Hsig, lines) and (f) wave propagation direction (vectors) weighted by Hsig^2. Two distinct seasons are delineated by the dashed magenta line.

3.6 Model experiments

Two model experiments, namely the Wind and wave (Case 1) and No wind or wave (Case 2) as detailed in Table 2, were undertaken to explore the intricate mechanisms shaping the impact of winds and waves on hydrodynamics and transport of riverine sediment. Case 1 encompassed a comprehensive wind and wave-current coupled experiment designed to emulate realistic conditions during simulation, achieved by integrating realistic wind inputs into the ROMS and SWAN models and specifying wave boundary conditions using nonstationary wave parameters derived from WAVEWATCH III model outputs. Conversely, Case 2 deliberately excluded any wind and wave effects by setting the wind speed to zero in both the ROMS and SWAN models and deactivating the wave boundary conditions. Consequently, the influence of waves and near-inertial motion induced by winds remained unaccounted for in Case 2.

Table 2. ROMS and SWAN model settings for different cases

Case ID	ROMS			SWAN	
	Discharges	Tides	Winds	Winds	BF
Wind and wave (Case 1)	✓	✓	✓	✓	✓
No wind or wave (Case 2)	✓	✓	×	×	×

Discharges refer to the freshwater and riverine sediment released from eight PRE outlets, BF refers to SWAN boundary forcing from the WWIII.

In Case 1, the surface roughness and surface stress contribution by waves were assessed using the method proposed by Drennan et al. (2005). Additionally, the wave-current bottom boundary module based on Madsen (1994), incorporated into COAWST, was activated to simulate the wave-current bottom boundary layer. The vortex force module of wave forces was also activated to compute the wave-induced momentum flux, utilizing the method proposed by McWilliams et al. (2004) and implemented in COAWST by Kumar et al. (2012). In both cases (Case 1 and Case 2), the bottom friction was computed based on a logarithmic velocity profile (Warner et al., 2008).

4 Results

4.1 Seasonal wave variations and its effects on bottom shear stress

Corresponding to the seasonal winds (Figure 3e), the seasonally-averaged wave characteristics in the PRE and the adjacent northern continental shelf of the South China Sea exhibit significant seasonal changes (Figure 4). During the wet summer season, the Hsig in these areas is relatively low, with waves predominantly coming from the southeast (Figure 4a). The seasonal average Hsig across the entire shelf remains below 1 m, with areas deeper than 60 m showing Hsig values above 0.8 m, while in shallower nearshore regions (water depth < 20 m), Hsig is less than 0.6 m (Figure 4a). Corresponding to the lower Hsig in the wet summer, the seasonally-averaged wave bottom orbital velocity (WBOV) is also relatively small, generally less than 1 cm s^{-1} in areas deeper than 40 m, except in some nearshore shallow water regions where it reaches up to 5 cm s^{-1} (Figure 4c). The seasonally-averaged bottom shear stress during the wet summer is relatively high in the PRE, nearshore regions, and the Taiwan Bank, where tidal dissipation is strong (Figure 4e). Compared to the No wind or wave case, the introduction of wind and waves leads to an increase in average bottom shear stress during the wet summer, particularly in regions where WBOV is significant, with an increase of approximately 0.05-0.1 Pa (Figure 4g).

https://doi.org/10.5194/egusphere-2024-3289
Preprint. Discussion started: 4 November 2024

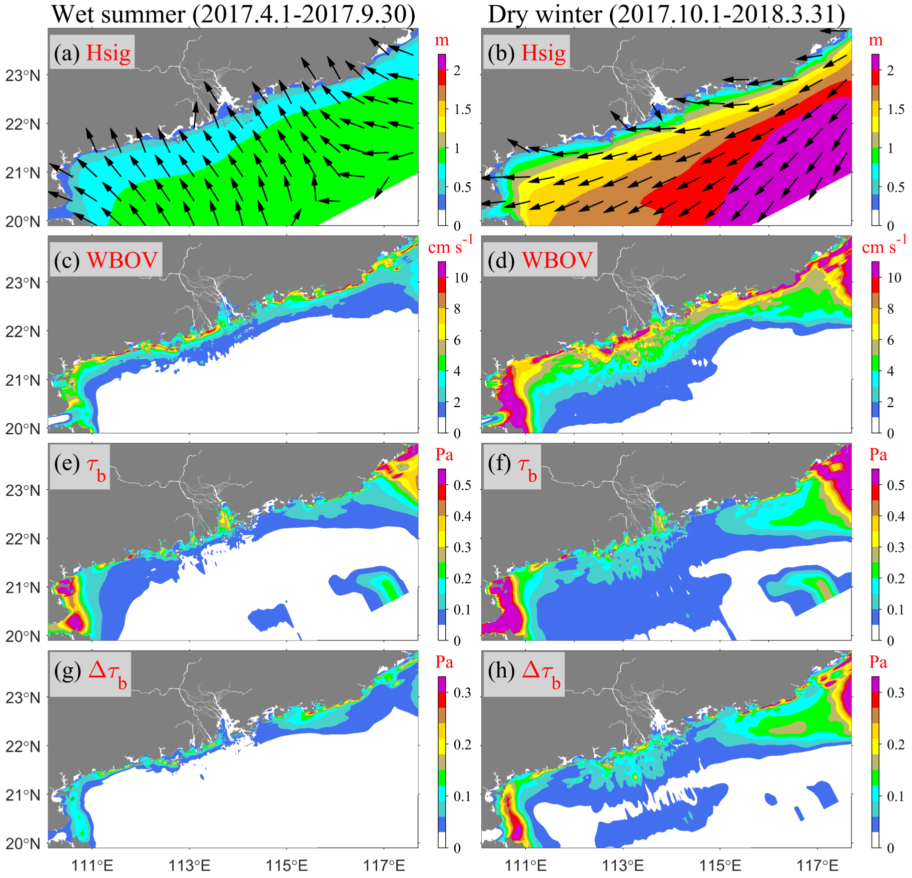

339

340 **Figure 4.** Patterns averaged over the entire wet summer season (from April 1st to
341 September 30th, 2017, as follows, Column 1) and the dry winter season (from
342 October 1st to March 31st, 2018, as follows, Column 2). Row 1 (a-b) for Hsig (color)
343 and propagation direction (vectors) weighted by Hsig^2, Row 2 (c-d) for wave bottom
344 orbital velocity (WBOV), Row 3 (e-f) for bottom shear stress magnitude in Case 1
345 (Wind and wave case). Row 4 (g-h) for bottom shear stress magnitude differences
346 between two cases (Case 1 minus Case 2).

347

https://doi.org/10.5194/egusphere-2024-3289
Preprint. Discussion started: 4 November 2024

In the dry winter season, Hsig in the study area increases significantly compared to the wet summer, with waves primarily coming from the northeast, although refraction occurs in some nearshore regions, changing the wave direction to southeast (Figure 4b). The area with water depths exceeding 60 m has a Hsig greater than 1.5 m, while in the 20-meter depth region, the Hsig reaches approximately 1 m (Figure 4b). Compared to the wet summer, the WBOV increases significantly in the PRE mouth and many nearshore regions, reaching up to 10 cm s^{-1} (Figure 4d). The average bottom shear stress on the continental shelf outside the estuary also increases significantly during the dry winter compared to the wet summer (Figure 4f). Since tidal intensity remains almost unchanged, the seasonal variation in tidal-induced stress is minimal, and the observed seasonal increase is mainly due to the stronger winter waves generating larger WBOV on the shelf. Compared to the No wind or wave case, the introduction of wind and wave in the dry winter leads to an increase in average bottom shear stress by approximately 0.1-0.15 Pa, with winter-averaged values reaching up to 0.3 Pa in areas such as the Taiwan Bank and east of the Leizhou Peninsula (Figure 4h).

4.2 Seasonal dispersal patterns of Pearl River plume and sediment

The residual sediment dispersal, flux, and deposition throughout the simulation period vividly illustrate patterns of sediment redistribution on an annual or seasonal scale. This section primarily focuses on illustrating the seasonally averaged fields of salinity, flow, riverine SSC, wind stress, depth-integrated riverine sediment flux, and riverine sediment deposition during the wet summer season (Figure 5) and dry winter season (Figure 6) on the continental shelf.

During the wet summer season, the discharge of freshwater and sediment from the Pearl River is substantial (Figure 3a), leading to a widespread expansion of the river plume into the sea (Figure 5a). The river plume expands both eastward and westward along the coast (Figure 5a). Due to the influence of southerly winds (Figure 5b), the speed of the river plume extending eastward is significantly higher than that extending westward.

In terms of riverine sediment suspension, its maximum turbidity zone (~100 mg L L^{-1}) is situated in the shallow water area near the estuary (water depth < 10 m). Beyond the estuary, suspended riverine sediment disperses across the shelf through the river plume. Further away from the estuary, its distribution aligns with that of the river plume, with concentrations diminishing as dispersal distance increases. Integrating the horizontal flux of river sediment vertically offers a clear indication of the primary transport pathway of riverine sediment (Figure 5c). Riverine sediment is predominantly transported westward and eastward. Westward coastal transport can extend as far as to the Leizhou Peninsula and Hainan Island. On the eastern side, eastward transport can reach Taiwan Bank. However, due to the obstruction of summer upwelling at Taiwan Bank, the transport path is diverted southward. The westward transport pathway is narrow and has a large magnitude of riverine sediment flux, while the eastward transport pathway is wide but the magnitude of riverine sediment flux is relatively weak. Throughout the wet summer season, substantial amounts of riverine sediment are deposited near the estuary (Figure 5d), particularly leading to notably high deposition of riverine sediment near the mouth bar (> 100 mm). Outside the estuary, the thickness of riverine sediment is comparatively lower, but it can reach approximately ~0.5 mm during the wet summer season in certain areas off the coast of western Guangdong.

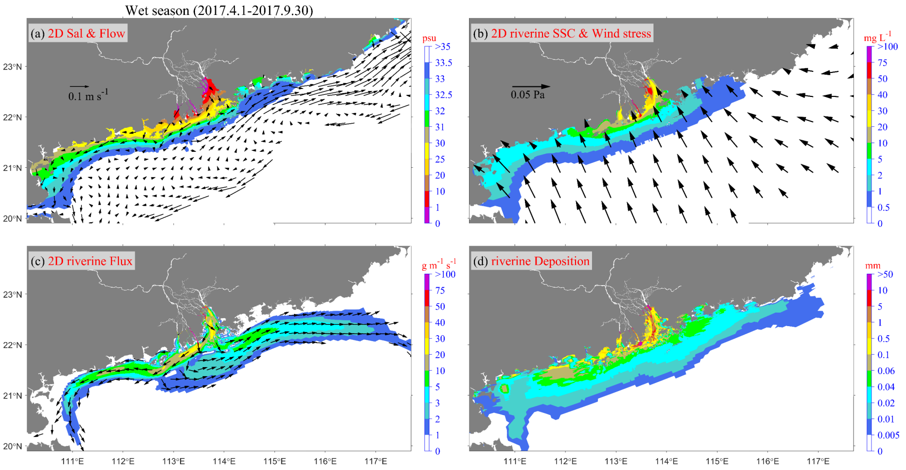

Figure 5. Patterns averaged over the entire wet summer season in Wind and wave case. (a) depth averaged salinity (color, psu) and flow (arrow, m s^{-1}). (b) depth averaged riverine SSC (mg L^{-1}). (c) depth-integrated riverine sediment transport rate (color, g m^{-1} s^{-1}) and direction (arrow). (d) riverine deposition thickness during the wet season (mm).

During the dry winter season, runoff from the Pearl River significantly decreases compared to the wet summer (as indicated in Figure 3a), accompanied by strong northeasterly winds. Consequently, the expansion of the Pearl River plume is constrained to the westward direction only, resulting in a narrow cross-shore width of the plume and the formation of a strong horizontal salinity gradient outside the estuary (Figure 6a). Flow velocity is increased near the salinity front, allowing river plume to extend westward through the Qiongzhou Strait to the Beibu Gulf. With sediment load during winter nearly negligible, the suspended concentration of riverine sediment is significantly lower compared to the wet summer (Figure 6b). In areas beyond the estuary, it is typically less than 5 mg L^{-1}, whereas inside the estuary, it is around ~10 mg L^{-1}. During the dry winter, following the transport path of river plume, riverine suspended sediment primarily moves westward along the coast, deflecting southward along the topography near the Leizhou Peninsula (Figure 6c). It then bifurcates near the east entrance of the Qiongzhou Strait, with one branch continuing into the Beibu Gulf, and the other branch proceeding southward along the east coast of Hainan Island. Stronger winds and waves in dry winter lead to the resuspension of a considerable amount of riverine sediments, originally deposited in estuaries and shelf seas during summer, which are then transported to coastal bays as well as to the sides and rear of the islands (Figure 6d). Additionally, a portion of the riverine sediment transported to the Beibu Gulf gets deposited on the seabed during the dry winter season.

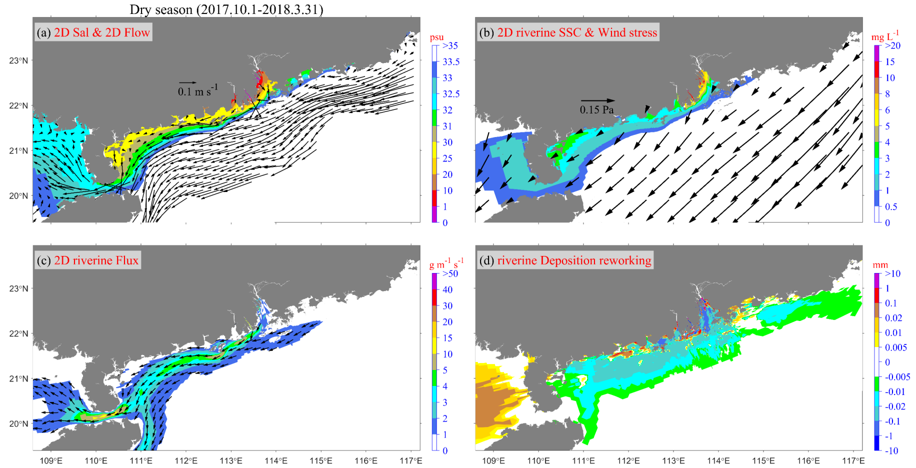

Figure 6. Same as Figure 5, but pertains to the dry winter season in Wind and wave case. Notably, (d) illustrates the variations in riverine sediment deposition on the seabed relative to the end of the wet summer season.

4.3 Annual dispersal pattern and the effect of winds and waves

In order to show the impact of winds and waves on the distribution of river plume and riverine sediment dispersal in a typical year, this section shows the results of two cases: Wind and wave (Figure 7) and No wind or wave (Figure 8).

In Wind and wave case, given the prevailing northeasterly wind stress throughout the year (Figure 7b), a significant portion of the river plume expands westward (Figure 7a). Similar to the expansion pattern of the river plume, the distribution of riverine suspended sediment is more concentrated near the estuary, with higher concentrations observed on the west side outside the estuary compared to the east side (Figure 7b). Horizontal transport of riverine suspended sediment outside the estuary involves both eastward and westward transport, with westward transport dominating and exhibiting a structure similar to that of winter transport (Figure 7c vs Figure 6c). Meanwhile, eastward transport follows a path similar to the eastern branch of the PRE plume observed during summer (Figure 7c vs Figure 5c). Consequently, Pearl River sediments are predominantly deposited near the estuary and in shallower water areas (water depth <40 m) on the east and west sides of the estuary (Figure 7d). Additionally, some riverine sediments are deposited in the Beibu Gulf area.

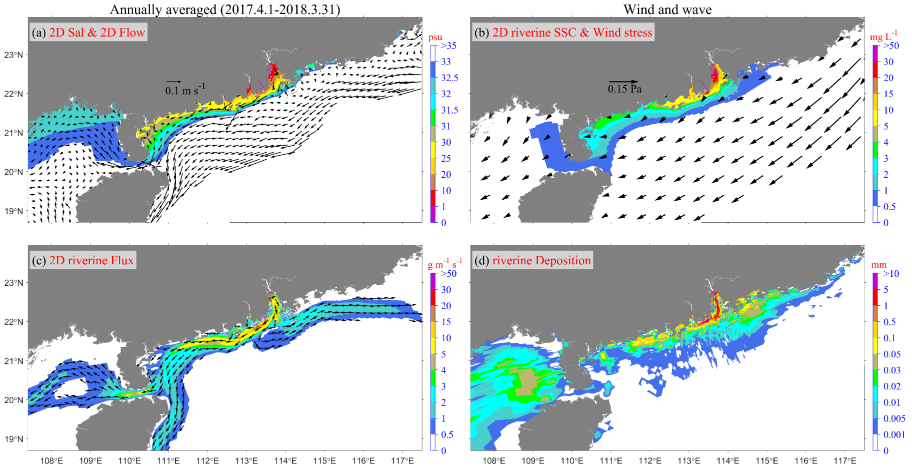

Figure 7. Same as Figure 5, but showcases the annual averaged patterns spanning from April 1st, 2017, to March 31st, 2018 in Wind and wave case.

In No wind or wave case, the river plume, characterized by a wider cross-shore width, primarily spreads toward the open sea due to the lack of wind and wave mixing (Figure 8a). This leads to pronounced stratification of the water column in the plume area. While riverine suspended sediment concentrations are higher near the estuary

(Figure 8b), riverine sediment is transported from the estuary outward and towards both the east and west sides, with the magnitude of eastward transport exceeding that of westward transport (Figure 8c). Riverine sediment deposition thickness in the estuary and near the mouth bar is relatively higher (Figure 8d), and the majority of riverine sediment transported outside the estuary gets deposited on the shelf not far from the estuary (water depth < 60 m).

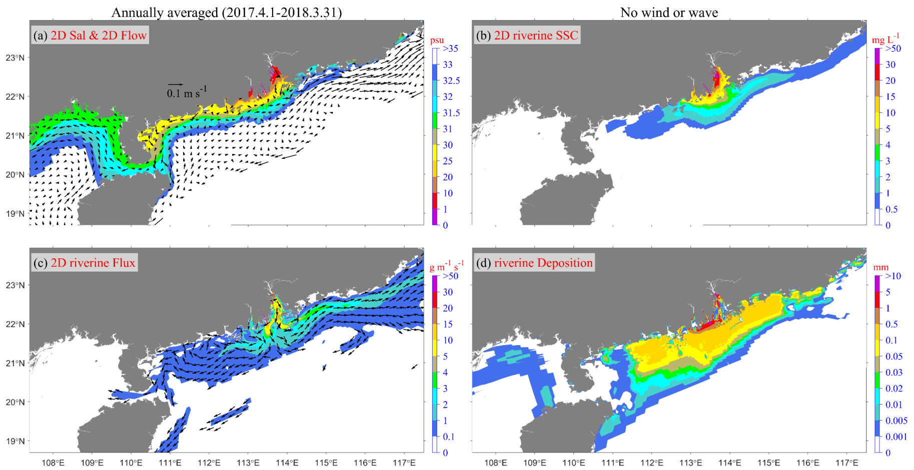

Figure 8. Same as Figure 7, but illustrates the annual averaged patterns under the condition of No wind or wave case.

In order to visually discern the vertical differences in hydrodynamics and sediment dynamics between the two scenarios, we examined the annually averaged conditions along the solid line section of the West transect shown in Figure 1a (Figures. 9-10). This transect is located precisely in the vicinity of the western outer side of the estuary, where westward transport is a fundamental characteristic in realistic conditions (Wind and wave case). The situations of this transect under both cases (Case 1 and 2) can effectively reflect the differences in hydrodynamics and sediment suspension, transport, and deposition processes.

In No wind or wave case, the river plume mainly concentrates in the surface layer of the water column (Figure 9a-b). The area where the river plume occupies has a water level about 2 cm higher than offshore (Figure 9a). There is a significant difference between surface and bottom salinity (Figure 9b), reaching 15 psu, resulting in a high buoyancy frequency (Figure 9f). The eddy viscosity and turbulent kinetic energy (TKE) are relatively low, with slightly higher values at the bottom and near the outer edge of the river plume (Figure 9e, g). Suspension and westward transport flux of riverine sediment primarily occurs in the nearshore and recirculation areas of the river plume bulge (Figure 9a-d), with lower concentrations offshore (Figure 9d). Due to the bottom shear stress generally being less than 0.1 Pa, with an average of 0.04 Pa, a large amount of sediment deposits across the entire transect, with an average of 0.16 mm (Figure 9h).

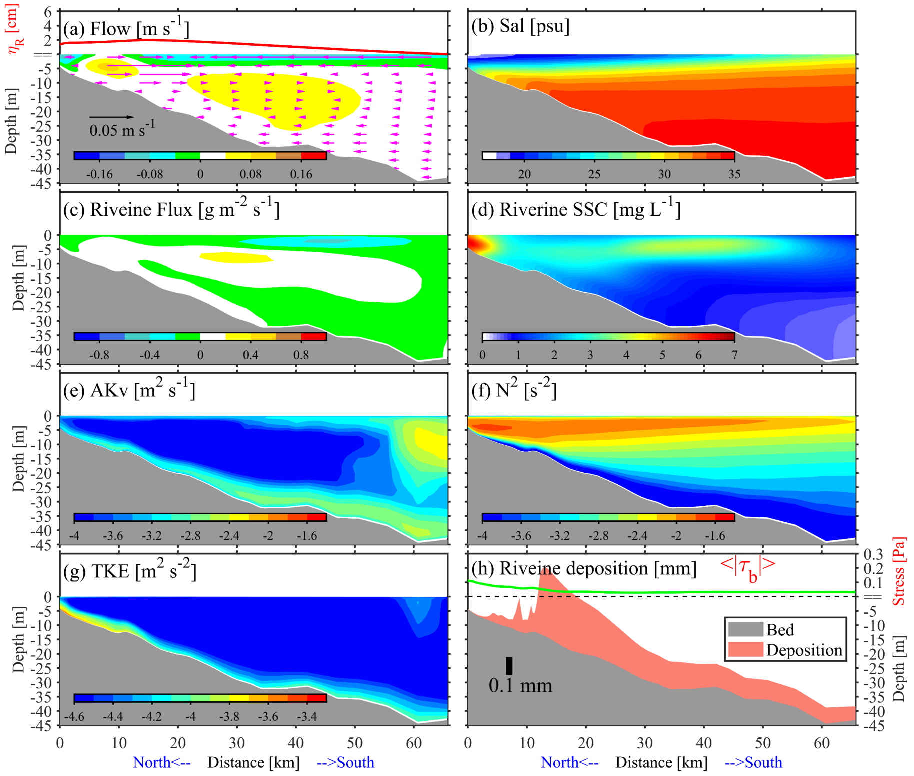

Figure 9. Annually averaged patterns at the solid part of the West transect in No wind or wave scenario. (a) alongshore (color), cross-shore (vector) direction velocity and relative sea level height (red solid line), (b) salinity, (c) axial riverine sediment flux, (d) riverine SSC, (e) logarithm of vertical viscosity coefficient (AKv), (f) logarithm of buoyancy frequency, (g) logarithm of turbulent kinetic energy (TKE), (h) riverine sediment deposition thickness and bottom stress magnitude (green solid line) at the seabed.

In Wind and wave case, the river plume extends offshore throughout the entire water column (Figure 10a-b). The wind causes the water level to elevate by 5 cm close to the coast compared to offshore areas, with a significant increase in westward surface flow velocity, much greater than under No wind or wave case (Figure 10a). The difference between surface and bottom salinity decreases to 7 psu, reducing the buoyancy frequency but increasing the horizontal salinity gradient across the shore (Figure 10b, f). Eddy viscosity increases significantly, especially in areas with higher salinity (Figure 10e). TKE also increases substantially, particularly in the surface layer affected by winds and waves and nearshore bottom layers affected by waves (Figure 10g). Suspension of riverine sediment is more pronounced in nearshore areas, with increased concentration, while concentrations decrease offshore (Figure 10d). The flux of riverine sediment transport towards the west significantly increases, primarily occurring in areas where westward flow intensifies (Figure 10c, a). Due to the overall increase in bottom shear stress, with an average of 0.11 Pa, sediment deposition thickness decreases dramatically to one-tenth of that under No wind or wave case (Figure 10h).

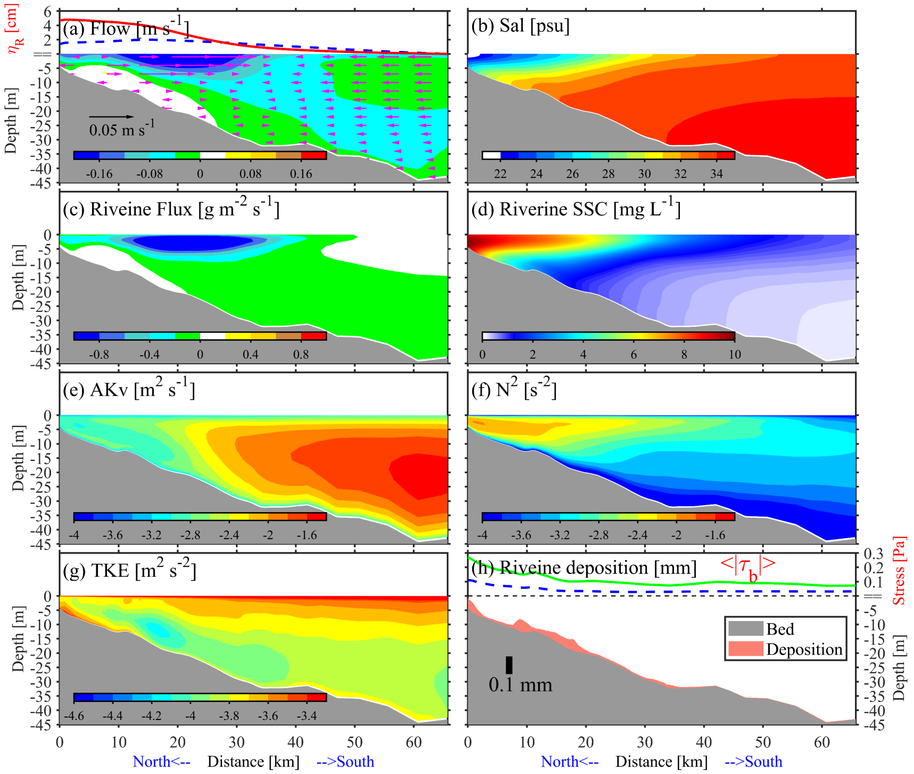

Figure 10. Same as Figure 9, but for the Wind and wave scenario. Note the blue dashed lines in (a) and (h) represent the relative sea level height and bottom stress magnitude in the No wind or wave scenario, respectively.

4.4 Riverine sediment Budget over the shelf with/without wind and wave effects

To improve the understanding of the spatial-temporal differentiation of riverine sediment dispersal, and the estimation of the fate of the Pearl River sediment during the wet summer season and throughout the year, we partitioned the model domain into eight distinct regions delineated by various transects as illustrated in Figure 1a. The division criteria are mainly based on the distance from the estuary and the natural separation by peninsulas and islands. These areas include:

① Near region: Proximity to the estuary,

② Eastern region: Eastern side of the estuary, closer to the shoreline,

③ Southeastern region: Further offshore on the eastern side of the estuary,

④ Southern region: Located deeper in the southern part of the estuary,

⑤ Western region: Western side of the estuary, closer to the shoreline,

⑥ Southwestern region: Offshore on the western side of the estuary,

⑦ Gulf region: Mainly the Beibu Gulf,

⑧ Far-off region: South of the Hainan Island.

By dividing the model domain into these delineated regions, we calculated the riverine sediment flux for each transect, thereby determining the total riverine sediment volume in each region. The riverine sediment flux data for different scenarios are presented in Table 3. Additionally, Figure 11 illustrates the proportion of riverine sediment retained within each region relative to the total river sediment input for the specific wet summer season or the whole year under two simulation cases.

Table 3. Time- and depth-integrated riverine sediment flux at the transects during different periods in two cases. (Unit: ×10^4 tons). Riverine sediment refers to the combined total of 'Clay (river)' and 'Silt (river)' as presented in Table 1.

Transect ID	Case ID	Wet summer	Dry winter	Yearlong
West solid	WW	-648.94	-292.09	-941.02
	NWW	-131.49	-51.50	-182.99
West dashed	WW	58.79	-136.67	-77.88
	NWW	-41.66	-105.21	-146.86
East solid	WW	470.24	-114.42	355.81
	NWW	410.99	41.04	452.04
East dashed	WW	12.91	-95.89	-82.98
	NWW	58.57	-9.73	48.84
South	WW	1.61	-2.83	-1.23
	NWW	-186.89	-46.98	-233.87
Shore	WW	-237.45	4.44	-233.01
	NWW	22.18	-53.90	-31.73
Coast	WW	-318.02	-503.84	-821.86
	NWW	0.27	12.32	12.59
Southwest	WW	-64.02	-351.33	-415.34
	NWW	-1.52	-44.87	-46.39
Strait	WW	-28.94	-419.36	-448.30
	NWW	-5.95	-18.53	-24.48
Bay	WW	4.82	-66.36	-61.54
	NWW	0.02	1.47	1.49

WW refers to Wind and wave, and NWW refers to No wind or wave.

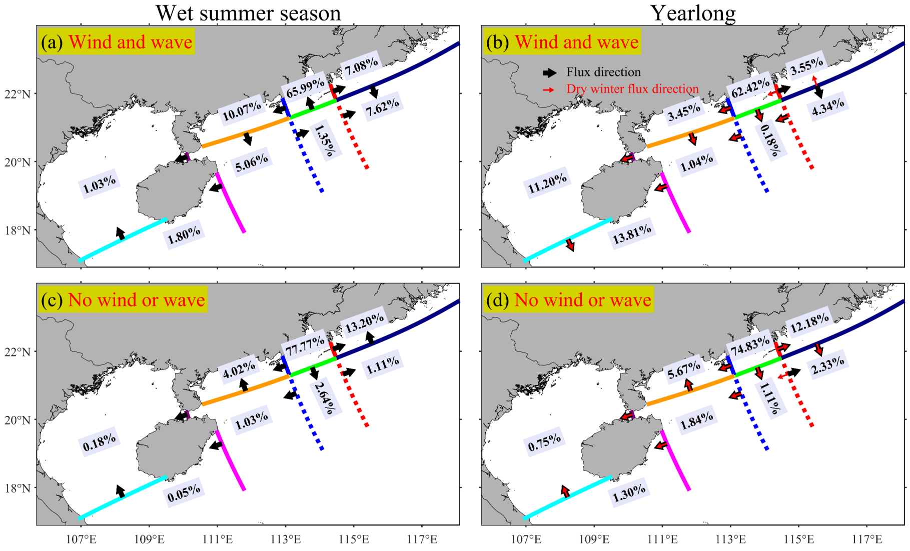

Figure 11. Riverine sediment retention at eight regions during the wet summer season (Column 1) and throughout the year (Column 2) across the Wind and wave case (Row 1) and No wind or wave case (Row 2). The arrows show the directions of riverine sediment flux at each transect during the specific period.

Combining the data from Table 3 with the results provided by Figure 11, it becomes apparent that the fate of Pearl River-derived sediment is intricately influenced by the presence or absence of winds and waves, as well as seasonal variations.

However, irrespective of Wind and wave conditions or seasonal changes, a predominant portion of riverine sediment is consistently retained within the "Near" region, proximal to the estuary, accounting for a substantial proportion ranging from 62.42% to 77.77% (Figure 11a-d).

In Wind and wave case, particularly in summer, the bulk of riverine sediment is transported onto the continental shelf east of the Qiongzhou Strait (Figure 11a). However, only a negligible fraction (2.83%) reaches the Beibu Gulf or the area south of Hainan Island. Interestingly, the quantity transported eastward (14.7%) is surpassed by the total amount transported westward (17.96%). Furthermore, the offshore area on the western side of the estuary retains a larger proportion (10.07%) of riverine sediment compared to the eastern side (7.08%).

A significant portion of the riverine sediment transported eastward is concentrated in the "Southeastern" region, attributable to the obstructive effect of the upwelling-plume front near shoals in eastern Guangdong and Taiwan Island during summer months (Chen et al., 2017a;Chen et al., 2017b). The encounter between river plume and upwelling results in the formation of a highly intense density front, generating strong jets along the front due to the thermal wind effect (Chen et al., 2019;Chen et al., 2017b).

In contrast, the winter season features strong northeasterly winds and strong waves, which significantly impact sediment dynamics across all six regions east of the Qiongzhou Strait (Figure 11b). Consequently, there is a marked increase in sediment retention within the "Gulf" and "Far-off" regions. These regions receive a combined total of 25% of the annual sediment input over the course of the year.

Notably, despite the occurrence of significant resuspension of riverine sediment within the "Near" region, minimal overall loss is observed. This phenomenon is attributed to the complex network of islands and coastlines present in the area. The intricate geography effectively traps the majority of the resuspended sediments behind islands or within the bay, preventing significant loss. Additionally, the "Near" region receives riverine sediment sourced from the adjacent "Eastern" region, further contributing to sediment retention within the area.

In No wind or wave case, water mixing is weakened, resulting in distinctive patterns of riverine sediment transport (Figure 11c-d). During the wet summer season, the substantial Pearl River freshwater discharge and riverine sediment load lead to a significant transport of riverine sediment, predominantly in a southward offshore direction (Figure 11c). Notably, the amount of riverine sediment transporting to the "Southern" region is doubled compared to the Wind and wave scenario, accounting for 2.64% of the total sediment load. Conversely, only 5.28% of sediment is transported westward of the estuary due to reduced bottom shear stress and westward currents in No wind or wave case.

Most of the riverine sediment tends to deposit near the estuary, with sediment deposited on the seabed exhibiting low susceptibility to resuspension. The exclusion of southeasterly winds during wet summer leads to a drastic decrease of more than two-thirds in westward sediment flux, with only a minimal fraction (0.23%) reaching the Beibu Gulf or the area south of Hainan Island. However, the eastward transport of riverine sediment experiences only a slight decrease to 14.31%, predominantly concentrated in the nearshore area due to reduced blocking effects caused by the exclusion of the summer monsoon and decreased upwelling.

Transitioning into the dry winter season, both the Pearl River freshwater

https://doi.org/10.5194/egusphere-2024-3289
Preprint. Discussion started: 4 November 2024

discharge and riverine sediment load decrease significantly, resulting in a reduction in the expansion range of the river plume. Furthermore, decreased shortwave radiation contributes to increased water mixing. Tidal effects in the "Near" region lead to the export of sediment to regions beyond its immediate vicinity, while strong tidal currents in the "Eastern" region facilitate the offshore transport of sediment to the "Southeastern" region (Figure 11d). Additionally, more riverine sediment is transported to the "Gulf" and "Far-off" regions during this period compared to the wet summer season when the downwelling-favorable winds are shut down.

5. Discussions

5.1 Mechanisms of Wind and Wave Effects on Hydro- and Riverine Sediment Dynamics

The suspension, transport, and deposition of the Pearl River sediment over the shelf are subject to changes associated with wind and wave effects (Figure 7-8), which have not been well addressed in previous research.

In No wind or wave case, the surface river plume can be swiftly transported outward from the estuary over long distances, but the riverine sediment primarily deposits in the nearby estuarine areas (Figure 8). When the wind and wave effects are present, the eastward transport of the plume diminishes, while the westward flow velocity increases (Figure 7). Correspondingly, riverine sediment transport towards the east decreases, while riverine sediment transport towards the west increases (Figure 7c vs Figure 8c). Riverine sediment deposition near the estuary decreases, while deposition in the Beibu Gulf significantly increases (Figure 7d vs Figure 8d).

This section analyzes the mechanisms of the riverine sediment dispersal from the perspectives of hydrodynamics and sediment dynamics (Figure 12 and 13).

It is evident that different paths of river plume movement correspond to Wind and wave and No wind or wave cases. Therefore, further momentum balance analysis of plume on these fast-moving paths is necessary, representing the force balance of movement under different scenarios. In the COAWST model, omitting the small vertical advection and horizontal viscosity, the momentum equation in the cross-shore direction (the Y-axis direction as showed in Figure 1b) is given by (Warner et al., 2008),

$$\underbrace{\frac{\partial v}{\partial t}}_{\text{ACC}} = \underbrace{-\frac{1}{\rho}\frac{\partial p}{\partial y}}_{\text{PGF}} \underbrace{-fu}_{\text{COR}} \underbrace{-\left(u\frac{\partial v}{\partial x}+v\frac{\partial v}{\partial y}\right)}_{\text{HADV}} \underbrace{+\frac{\partial}{\partial z}\left(Akv\frac{\partial v}{\partial z}\right)}_{\text{VVSIC}} \underbrace{+WT}_{\text{wave-induced}} \qquad (1)$$

where u and v are the velocities in the X-axis (alongshore) and Y-axis direction, respectively; ρ is the sea water density; f is the Coriolis parameter; and Akv is the vertical eddy viscosity. The terms from left to right denote the acceleration (ACC), pressure gradient (PGF), Coriolis force (COR), horizontal advection (HADV), vertical mixing (VVSIC, surface stress SSTR, and bottom stress BSTR terms when in two dimensions), and wave-induced forces (i.e., wave breaking and roller force, horizontal vortex force and Coriolis-Stokes force terms). The momentum terms are averaged in 365 days to see the yearlong mean pattern.

In No wind or wave case, the annually averaged currents on the eastern side of the PRE primarily experience the COR and PGF in the cross-shore direction, with the remaining terms being minor and not shown (Figure 12a, c). The PGF is directed shoreward, while the COR is directed seaward, resulting in a geostrophic balance. Significant water level gradients at the surface correspond to a strong eastward geostrophic flow ($u_g = -gf^{-1}\partial\eta/\partial y$), consistent with the annual average eastward flow field (Figure 12e and Supplement Figure S4o). The eastward flow is mainly driven by the thermal wind effect ($\partial u/\partial z = g\rho_0^{-1}f^{-1}\partial\rho/\partial y$, where g, ρ, and ρ_0 are the acceleration of gravity, the seawater density, and averaged seawater density, respectively), as river plume encounters upwelling, forming a strong density front with notable vertical velocity shear (Figure 12g). In the region south of the plume-upwelling front, vertical velocity shear supports westward plume movement or dampens its eastward velocity.

In Wind and wave case, on one hand, the onshore Ekman transport ($-\rho_0^{-1}f^{-1}\tau_x$, τ_x is the wind stress in the alongshore direction) due to annually averaged northeasterly winds leads to an increase in nearshore water levels on the western side of PRE, causing the currents to tend towards the west, forming geostrophic currents (Figure 12f). On the other hand, northeast winds generate westward wind stress, resulting in westward wind-driven currents (Figure 7a). Additionally, density fronts south of the plume can create strong westward vertical velocity shear (Figure 12h). These factors contribute to the rapid westward movement of the plume. After the adjustment of water levels, the surface geostrophic currents approximate geostrophic balance in the cross-shore direction (Figure 12b and d).

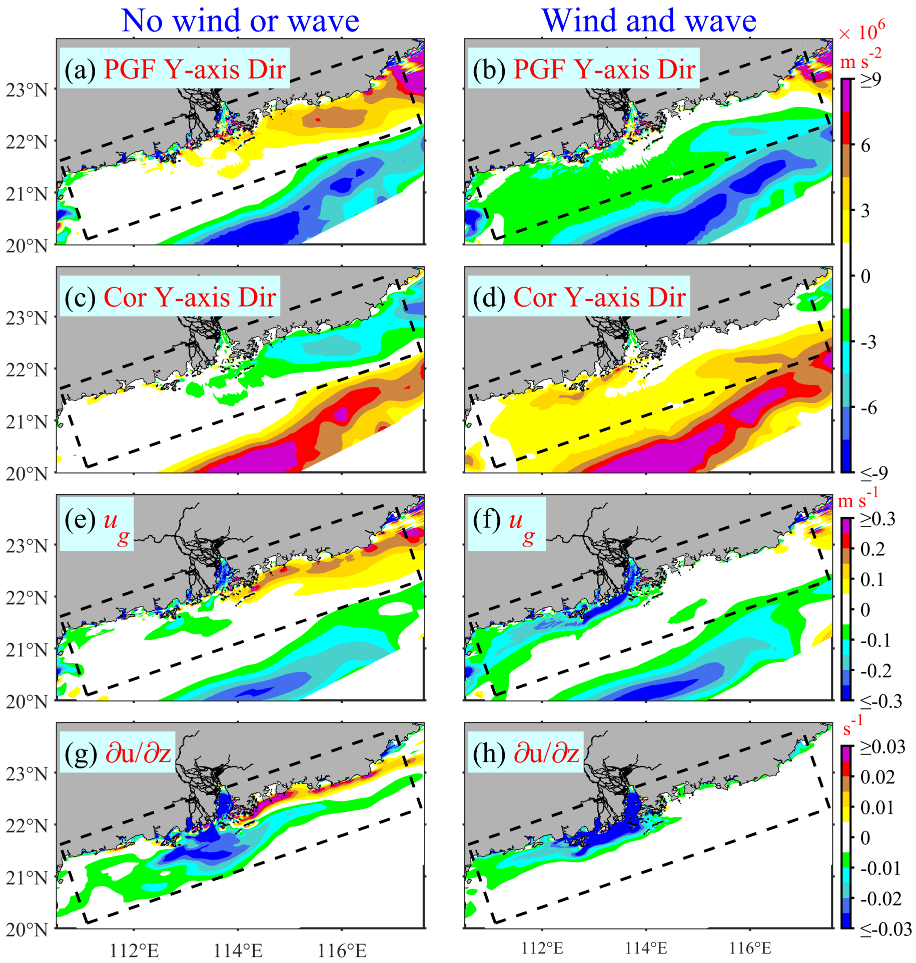

Figure 12. (a-b) Pressure gradient term in the Y-axis direction, (c-d) Coriolis force term in the Y-axis direction, (e-f) geostrophic velocity in the X-axis direction derived from the geostrophic balance equation, (g-h) vertical velocity shear at surface layer in the X-axis direction derived from the thermal wind equation. No Wind or wave (Column 1) and Wind and wave (Column 2) scenario, respectively.

The preceding analysis involves the dynamic mechanisms governing plume spreading paths under both Wind and wave and No wind or wave cases. Now, we turn to analyze the riverine sediment transport mechanisms under varying dynamic conditions. To accomplish this, we examined the annual and depth-averaged sediment transport terms under two scenarios. By excluding minor vertical advection and diffusion factors, the sediment transport equation (Warner et al., 2008) can be represented as follows:

$$\underbrace{\frac{\partial C}{\partial t}}_{\text{Rate}} = \underbrace{-\frac{\partial uC}{\partial x} - \frac{\partial vC}{\partial y}}_{\text{HADV of SSC}} \underbrace{-\frac{\partial w_s C}{\partial z}}_{\text{Settling}} \underbrace{+E_0\left(1-\phi\right) max(\frac{\tau_b - \tau_{ce}}{\tau_{ce}},0)}_{\text{Resuspension}} \qquad (2)$$

where C represents the SSC; w_s is the settling velocity (positive upwards); E_0 indicates a bed erodibility parameter (kg m^{-2} s^{-1}); ϕ is the porosity (volume of voids/total volume) of the top bed layer; τ_b and τ_{ce} are the bottom shear stress and critical shear stress for erosion, respectively. The terms from left to right denote the rate of change in SSC (rate), the lateral sediment advection (HADV of SSC), vertical settling (Settling), and the bottom erosion (Resuspension), respectively.

In No wind or wave case, riverine sediment is transported horizontally to the outer region of the PRE and distributed to both the east and west sides of the PRE (Figure 8c and 13a), thereby increasing the riverine SSC outside the estuary (Figure 8b). These riverine sediments continuously deposit on the seabed during transportation (Figure 8d and 13b), while resuspension primarily occurs in areas with strong tidal currents and high bottom shear stress, such as the PRE, the north side of the Taiwan Bank, and near the Leizhou Peninsula (Figure 13c). Consequently, net deposition (Settling + Resuspension) primarily occurs in shallow areas close to the PRE where bottom shear stress is low (Figure 8d, Supplement Figure S4m, and Figure 13d), while suspension dominates in areas with high shear stress.

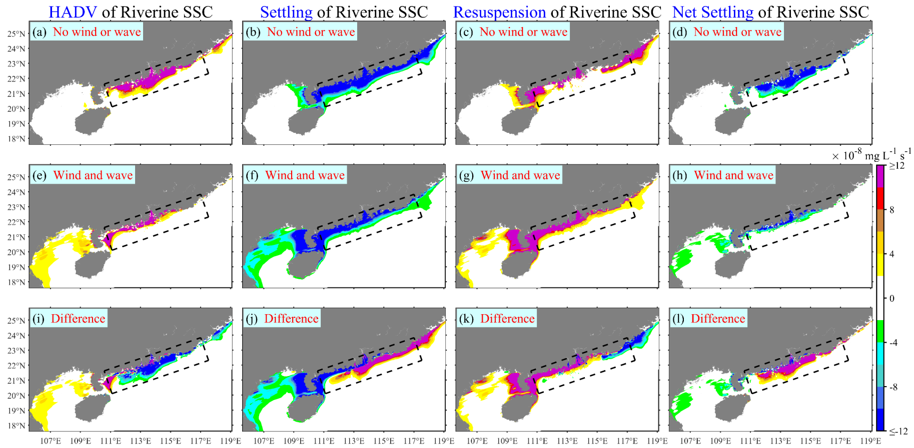

Figure 13. Annually averaged patterns of riverine SSC diagnostic term (a, e, i) horizontal total advection, (b, f, j) vertical settling, (b, f, j) resuspension, (b, f, j) net settling calculated by vertical settling in addition to resuspension. No Wind or wave (Row 1), Wind and wave (Row 2) scenario, and the difference between them (Wind and wave minus No Wind or wave, Row 3), respectively.

In Wind and wave case, riverine sediment mainly transports westward after exiting the PRE (Figure 7c and Figure 13e), with significantly reduced net transport fluxes towards the east and south. Meanwhile, the bottom shear stress increases on both the east and west sides adjacent to the PRE (Supplement Figure S4m-n), leading to increased resuspension. In regions further north of the Taiwan Bank, sediment deposition and resuspension decrease due to reduced transport of riverine sediment to these areas (Figure 13g, k). Eventually, resuspension significantly increases in most

https://doi.org/10.5194/egusphere-2024-3289
Preprint. Discussion started: 4 November 2024

areas east of the Leizhou Peninsula, accompanied by a substantial decrease in sediment deposition thickness (Figure 7d and Figure 13l). Most of the riverine sediment due to reduced retention is transported to the sides of the Leizhou Peninsula and the Beibu Gulf (Figure 7d and Figure 13l).

Overall, wind and wave dynamics are pivotal in shaping coastal hydrodynamics and riverine sediment dispersal patterns. Wind significantly influences flow, while waves notably affect resuspension. Together, they impact riverine sediment transport and deposition on the continental shelf of the northern South China Sea.

5.2 Comparison with previous studies and implications for future morphological evolution of the shelf

The fate of sediment dispersed from the river into the coastal ocean involves at least four processes: supply via plumes; initial deposition; resuspension and transport by marine processes; and long-term net accumulation (Wright and Nittrouer, 1995). In general, a significant proportion of river sediment tends to deposit in the estuary and its vicinity (Walsh and Nittrouer, 2009;Hanebuth et al., 2015). Walsh and Nittrouer (2009) present a hierarchical decision tree designed to predict the marine dispersal system at a river mouth based on fundamental oceanographic and morphological characteristics. Within this framework, the fate of riverine sediment deposition can be determined using key factors such as riverine sediment discharge, shelf width, and wave and tidal conditions.

Although the Pearl River's riverine sediment discharge exceeds 2 megatons per year, most of the sediment remains deposited near the estuary, indicating an estuarine accumulation-dominated system. This is likely due to a combination of factors, including the wide mouth of the estuary, large accommodation space of the estuary, the presence of numerous nearby islands, and weak tidal forces. For the PRE, Chen et al. (2023) utilized high-resolution seismic data to discover that, since approximately 7.5 ka BP, only around 35% of the sediment derived from the Pearl River has dispersed to offshore shelf areas from the delta-estuary system. Our research indicates that the majority of Pearl River sediment deposits are near the PRE, with the remaining 38% being transported to other areas, which is consistent with the findings of Chen et al. (2023). Outside the estuary, the continental shelf extends well beyond the 12 km threshold to over 100 km in width. As a result, most escaped riverine sediments tend to accumulate on the shelf rather than being captured by submarine canyons. This wide, shallow shelf promotes sediment deposition and limits the direct transport of fine sediments into deeper waters (Walsh and Nittrouer, 2009).

Unlike the hierarchical decision tree proposed by Walsh and Nittrouer (2009), where sediment deposition can be categorized based on wave and tidal conditions, the PRE does not fit neatly into this framework. Whether deposition is dominated by proximal or distal processes cannot be fully determined by annually-averaged waves and tides alone. In the PRE, proximal deposition predominantly occurs during the wet summer, when winds and waves are relatively weak. In contrast, distal deposition is more prominent in the dry winter, driven by strong northeasterly winds and high waves.

Indeed, the PRE and adjacent shelf exhibits a fascinating seasonal dynamics where sediment delivery and sediment remobilization occur at different times of the year. During the summer wet season, the region experiences substantial sediment delivery due to high river discharge from the Pearl River, bringing a large influx of riverine sediments to the shelf. Conversely, in winter, when strong waves driven by northeast monsoon winds dominate, riverine sediment remobilization becomes the key process. These high-energy waves increase bottom shear stress, resuspend previously deposited sediments and redistribute them across the shelf, especially in sheltered areas like the Beibu Gulf.

Other estuaries exhibit similar multiple-step sediment delivery and dispersal patterns, such as the Mekong River Estuary. In these systems, sediment transport is not confined to a single process but rather occurs in stages, influenced by seasonal variations in hydrodynamic conditions. Like the PRE, the Mekong experiences distinct phases of sediment deposition, with fine sediments being delivered during periods of high river discharge and then redistributed by waves and tidal forces, particularly during monsoonal shifts (Xue et al., 2012;Eidam et al., 2017). These complex patterns highlight the interplay between riverine inputs, coastal morphology, and oceanographic processes in shaping sediment dynamics.

These sediment delivery patterns have implications beyond sediment fate, particularly for carbon cycling. Sediment deposition in coastal and shelf areas plays a significant role in trapping organic carbon, influencing long-term carbon burial rates (LaRowe et al., 2020). Sediment dynamics directly influence the fate of organic carbon (OC) in marine environments, where sediments function as both a sink and a source of OC, playing a pivotal role in global carbon cycling (Repasch et al., 2021).

The multiple-step transport mechanisms can lead to varying carbon storage locations, affecting the sequestration potential of these systems. Additionally, resuspension and redistribution of sediments, especially during high-energy events, may expose previously buried organic material, leading to carbon remineralization and influencing coastal nutrient cycles and ecosystem health (Ståhlberg et al., 2006;Moriarty et al., 2018). Therefore, understanding these patterns is crucial for assessing the broader impacts on carbon cycling and coastal biogeochemical processes.

Our results indicate that during the wet summer period, 14.7% of river sediment can be transported to the southeast side of the PRE, with approximately half of it still retained on the eastern side of the PRE during the following dry winter, forming a proximal mud belt. However, due to winter winds and wave reshaping, the thickness of the riverine sediment deposition in the distal mud belt significantly decreases, with only one-third of the riverine sediment deposited in the wet summer period being retained during the ensuing dry winter. Our results indicate that 11.2% of the Pearl River's riverine sediment can be transported to the Beibu Gulf under the Wind and wave case, confirming the speculation by Ge et al. (2014) and validating the conclusions estimated by Lin et al. (2020). From a hydrodynamic perspective, Shi et al. (2002) found that the net flux of currents in the Qiongzhou Strait is westward throughout the year. Our results for both wet summer and dry winter currents in the Qiongzhou Strait are consistent with Shi et al. (2002). This westward flow contributes to the westward transport of Pearl River sediment to the Beibu Gulf.

Our results highlight the wind and wave effects on the riverine sediment suspension, resuspension, transport, and net deposition during a typical year. We've developed a conceptual diagram illustrating the wind and wave effects on shelf hydrodynamics and riverine sediment dynamics based on our model results (Figure 14). When there is no wind or wave, strong stratification occurs, causing the plume to expand outward from the surface, with low TKE and bottom shear stress, resulting in weak resuspension (Figure 14a, c). Most of the riverine sediment deposits near the estuary, while the strong tidal-induced upwelling to the east of the estuary triggers the eastward expansion of the plume (Figure 14a). Under the wind and wave effects, TKE and eddy viscosity increase, stratification weakens, and during the summer southerly monsoon, the upwelling area to the east of the estuary expands (Figure 14b, d). This leads to some of the riverine sediment being transported southeastward along the edge of the upwelling-plume interface (Figure 14b). Ekman transport causes an increase in the cross-shore gradients of water level, salinity, and density to the west of the estuary, triggering stronger geostrophic currents and vertical shear (Figure 14d). With increased bottom TKE and shear stress by wave, resuspension strengthens and net deposition decreases, resulting in higher riverine SSC and a significant increase in the westward riverine sediment flux, compounded by the intensified westward flow. As a result, more Pearl River sediments are transported to the Beibu Gulf (Figure 14b). Due to the sheltering effect of the Leizhou Peninsula against the northeast winds and waves, these sediments are more likely to settle on the seafloor in the Beibu Gulf region compared to those on the continental shelf east of the Leizhou Peninsula.

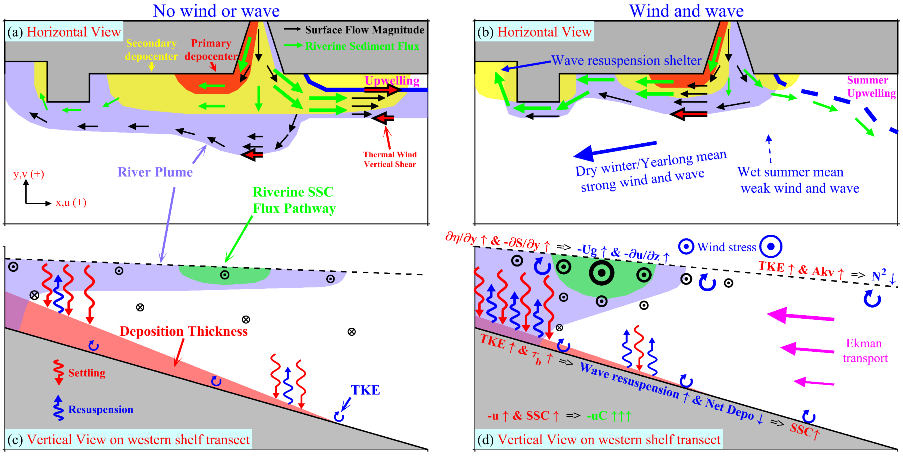

Figure 14. Schematic of the wind and wave effects on river plume dynamics and riverine sediment dispersal dynamics over the shelf. The first column represents No wind or wave conditions, while the second column represents Wind and wave conditions. The first row denotes horizontal distribution, and the second row denotes vertical distribution of the cross-shore transect on the western shelf.

5.3 Limitations and Future Work

This study has focused on analyzing simulation results from a typical year, encompassing both wet and dry seasons from 2017 to 2018, to understand the seasonal variations and annual patterns of suspension, transport, and deposition of sediment in the PRE and adjacent shelf. However, it's essential to recognize that the long-term sediment transport and deposition dynamics in the Pearl River are influenced by numerous complex factors. These include changes in sea level and coastal line (Harff et al., 2010;Church and White, 2006;Hong et al., 2020), alterations in wind field and precipitation (Ning and Qian, 2009;Young et al., 2011), natural sedimentation within the Pearl River Delta (Wu et al., 2010), modifications in sediment load and underwater volume of the estuary caused by anthropogenic impact (Wu et al., 2018;Wu et al., 2014;Lin et al., 2022). Therefore, while this study sheds light on seasonal and annual timescale patterns, it cannot fully represent the short or long-term transport and deposition trends of the Pearl River sediment. Yet for many shelf systems, a lot of the sediment transport happens during short lived events. Consideration of the episodicity of transport would be helpful for future studies.

Additionally, it's important to note that this article primarily focuses on the fate of the Pearl River sediment on the inner shelf. However, there are other smaller rivers within the Pearl River plume's expansion range, like the Han River, Rong River, Moyang River, Jian River, and Nandu River (Liu et al., 2016). Although these rivers contribute less freshwater and sediment compared to the Pearl River, they still impact seawater salinity, suspended sediment concentration, and seabed geomorphology (Wang et al., 2023;Zong et al., 2024). Hence, there is a need for further systematic research to understand the processes and impacts of these smaller rivers comprehensively.

Lastly, while the model used in this study has shown good validation results, conducting numerous sensitivity experiments on sediment parameters, such as settling velocity and critical erosion stress, would be beneficial. Settling velocity can influence the location of sediment depocenters, with higher settling velocities leading to more sediment entrapment and older sediment age in the estuary and vice versa (Zhu et al., 2020;Ralston and Geyer, 2017;Zhu et al., 2021). Similarly, critical erosion stress can affect the resuspension of deposited sediment, with higher critical erosion stress resulting in less resuspension and more deposition especially during neap tides and weak wind wave events (Choi et al., 2023;Dong et al., 2020). Conducting such sensitivity analyses would enhance our understanding of sediment dynamics in estuaries and shelves. Besides, the model does not account for cohesive processes, such as consolidation and flocculation, which can significantly impact sediment behavior (Sherwood et al., 2018). Our model does not incorporate wave and current-supported gravity flows, which are important factors influencing sediment transport in submarine canyon areas (Harris et al., 2005;Ma et al., 2010;Zhang et al., 2020). Since our study area primarily focuses on the continental shelf and the simulated results indicate that sediment transport occurs mainly in the shallow inner shelf, where canyons are relatively rare, this omission has a relatively minor impact on our results.

6. Conclusions

This study utilizes the COAWST model to quantitatively analyze the suspension, transport, and ultimate fate of Pearl River-derived sediment on the continental shelf over a typical year, capturing key marine variables such as water level, wave height, flow velocity, salinity, temperature, and SSC.

The study indicates that approximately 62% of riverine sediment remains near the estuary annually. During the wet summer, calm conditions foster initial sediment deposition via the river plume. Conversely, winter's stronger winds and waves resuspend and transport sediments into Beibu Gulf, primarily during this dry season.

Overall, sediment predominantly follows a southwestward pathway, with wind and wave interactions diminishing proximal riverine sediment deposition levels to 83% of those in No wind or wave conditions, resulting in a remarkable fivefold increase in westward alongshore sediment flux.

The model indicates that wind dynamics significantly impact both surface and bottom boundary layers, enhancing vertical mixing and bottom shear stress, which raises nearshore SSC while decreasing offshore SSC and sediment deposition thickness. Enhanced cross-shore gradients of water level and density further promote westward geostrophic flow, facilitating sediment transport to more distant areas. This research offers novel insights into the complex interactions between wind, waves, and riverine sediment dynamics on continental shelves.

Acknowledgments

This research was funded by the National Natural Science Foundation of China (grant numbers 42306015 and 42276169), the China Postdoctoral Science Foundation (grant number 2023M743988). Wenping Gong is supported by the Southern Marine Science and Engineering Guangdong Laboratory (Zhuhai) (SML2023SP238). The authors would like to thank the crew of the R/V Changhe Ocean for their valuable contribution during collection of the field-data.

Data availability

The HYbrid Coordinate Ocean Model outputs are from: http://hycom.org/hycom. The NCEP Climate Forecast System Version 2 (CFSv2) reanalysis data can be obtained at the following website: https://rda.ucar.edu/datasets/ds094.1/dataaccess/.

The WAVEWATCH III wave model output fields can be downloaded from: ftp://polar.ncep.noaa.gov/pub/history/waves. Hourly water-level data observed at Quarry Bay station are provided by the Hong Kong Observatory website: https://www.hko.gov.hk/sc/tide/marine/realtide.htm?s=QUB&t=TABLE. The mooring data for the S1 station are sourced from Liu et al. (2023). The field- and numerical data used in this paper can be downloaded from: https://doi.org/10.5281/zenodo.13740968.

Declaration of Competing interests

The authors declare that there are no competing interests among any of the authors.

CRediT authorship contribution statement

Guang Zhang: Conceptualization, Numerical modeling, Validation, Data visualization, Writing - original draft, and Funding acquisition. **Suan Hu:** Writing - review & editing. **Xiaolong Yu:** Writing - review & editing. **Heng Zhang:** Writing - review & editing. **Wenping Gong:** Writing - review & editing, and Funding acquisition

Supplement:

We have included the validation and analysis of the model's water levels, Hsig, flow velocities, salinity, temperature, and SSC, as well as the spatial results and analysis of annual averages for various oceanic elements from two cases used to support the discussion, in the Supplement file.

References

Bever, A. J., Harris, C. K., Sherwood, C. R., and Signell, R. P.: Deposition and flux of sediment from the Po River, Italy: An idealized and wintertime numerical modeling study, Marine Geology, 260, 69-80, 10.1016/j.margeo.2009.01.007, 2009.

Burchard, H., Schuttelaars, H. M., and Ralston, D. K.: Sediment Trapping in Estuaries, Annual Review of Marine Science, 10, 371-395, 10.1146/annurev-marine-010816-060535, 2018.

Cao, L., Liu, J., Shi, X., He, W., and Chen, Z.: Source-to-sink processes of fluvial sediments in the northern South China Sea: Constraints from river sediments in the coastal region of South China, Journal of Asian Earth Sciences, 185, 104020, 10.1016/j.jseaes.2019.104020, 2019.

Chapman, D. C.: Numerical Treatment of Cross-Shelf Open Boundaries in a Barotropic Coastal Ocean Model, Journal of Physical Oceanography, 15, 1060-1075, 1985.

Chen, Y., Deng, B., Saito, Y., Wang, Z., Yang, X., and Wu, J.: Pearl River sediment dispersal over its associated delta–estuary–shelf system during the Holocene, Sedimentology, 70, 2331-2354, 10.1111/sed.13123, 2023.

Chen, Z., Pan, J., and Jiang, Y.: Role of pulsed winds on detachment of low salinity water from the Pearl River Plume Upwelling and mixing processes, Journal of Geophysical Research: Oceans, 121, 2769-2788, 10.1002/2015JC011337, 2016.

Chen, Z., Gong, W., Cai, H., Chen, Y., and Zhang, H.: Dispersal of the Pearl River plume over continental shelf in summer, Estuarine, Coastal and Shelf Science, 194, 252-262, 10.1016/j.ecss.2017.06.025, 2017a.

Chen, Z., Pan, J., Jiang, Y., and Lin, H.: Far-reaching transport of Pearl River plume water by upwelling jet in the northeastern South China Sea, Journal of Marine Systems, 173, 60-69, 10.1016/j.jmarsys.2017.04.008, 2017b.

Chen, Z., Jiang, Y., Wang, J., and Gong, W.: Influence of a River Plume on Coastal Upwelling Dynamics: Importance of Stratification, Journal of Physical Oceanography, 49, 2345-2363, 10.1175/jpo-d-18-0215.1, 2019.

Chi, Y., and Rong, Z.: Effects of Breaking and Non-Breaking Surface Wave Mixing on the Changjiang River Plume Dynamics in Summer, Journal of Geophysical Research: Oceans, 128, 10.1029/2022jc019501, 2023.

Choi, S. M., Seo, J. Y., and Ha, H. K.: Contribution of local erosion enhanced by winds to sediment transport in intertidal flat, Marine Geology, 465, 107171, 10.1016/j.margeo.2023.107171, 2023.

Church, J. A., and White, N. J.: A 20th century acceleration in global sea-level rise, Geophysical Research Letters, 33, n/a-n/a, 10.1029/2005gl024826, 2006.

Dong, H., Jia, L., He, Z., Yu, M., and Shi, Y.: Application of parameters and paradigms of the erosion and deposition for cohesive sediment transport modelling in the Lingdingyang Estuary, China, Applied Ocean Research, 94, 101999, 10.1016/j.apor.2019.101999, 2020.

Dong, L., Su, J., Wong, L., Cao, Z., and Chen, J.: Seasonal variation and dynamics of the Pearl River plume, Continental Shelf Research, 24, 1761-1777, 10.1016/j.csr.2004.06.006, 2004.

Drennan, W. M., Taylor, P. K., and Yelland, M. J.: Parameterizing the sea surface roughness, Journal of Physical Oceanography, 35, 835-848, Doi 10.1175/Jpo2704.1, 2005.

Dyer, K. R.: Estuaries: A Physical Introduction, 2nd Edition, John Wiley & Sons, Chichester, 195 pp., 1997.

Egbert, G. D., and Erofeeva, S. Y.: Efficient inverse Modeling of barotropic ocean tides, Journal of Atmospheric and Oceanic Technology, 19, 183-204, Doi 10.1175/1520-0426(2002)019<0183:Eimobo>2.0.Co;2, 2002.

Eidam, E. F., Nittrouer, C. A., Ogston, A. S., DeMaster, D. J., Liu, J. P., Nguyen, T. T., and Nguyen, T. N.: Dynamic controls on shallow clinoform geometry: Mekong Delta, Vietnam, Continental Shelf Research, 147, 165-181, 10.1016/j.csr.2017.06.001, 2017.

Flather, R. A.: A tidal model of the north-west European continental shelf, Memoires Societe Royale des Sciences de Liege, 10, 141-164, 1976.

Gan, J., Cheung, A., Guo, X., and Li, L.: Intensified upwelling over a widened shelf in the northeastern South China Sea, Journal of Geophysical Research, 114, 10.1029/2007jc004660, 2009.

Gan, J., San Ho, H., and Liang, L.: Dynamics of Intensified Downwelling Circulation over a Widened Shelf in the Northeastern South China Sea, Journal of Physical Oceanography, 43, 80-94, https://doi.org/10.1175/JPO-D-12-02.1, 2013.

Gao, X., Chen, S., Xie, X., Long, A., and Ma, F.: Non-aromatic hydrocarbons in surface sediments near the Pearl River estuary in the South China Sea, Environmental Pollution, 148, 40-47, 10.1016/j.envpol.2006.11.001, 2007.

Gao, X., Arthur Chen, C.-T., Wang, G., Xue, Q., Tang, C., and Chen, S.: Environmental status of Daya

Bay surface sediments inferred from a sequential extraction technique, Estuarine, Coastal and Shelf Science, 86, 369-378, 10.1016/j.ecss.2009.10.012, 2010.

Ge, Q., Liu, J. P., Xue, Z., and Chu, F.: Dispersal of the Zhujiang River (Pearl River) derived sediment in the Holocene, Acta Oceanologica Sinica, 33, 1-9, 10.1007/s13131-014-0407-8, 2014.

Ge, Q., Xue, Z., Yao, Z., Zang, Z., and Chu, F.: Anti-phase relationship between the East Asian winter monsoon and summer monsoon during the Holocene?, Journal of Ocean University of China, 16, 175-183, 10.1007/s11802-017-3098-x, 2017.

Ge, Q., Xu, D., Ye, L., Yang, K., and Yao, Z.: Linking Monsoon Activity with River-Derived Sediments Deposition in the Northern South China Sea, Journal of Ocean University of China, 18, 1098-1104, 10.1007/s11802-019-4155-4, 2019.

Geyer, W. R., Hill, P. S., and Kineke, G. C.: The transport, transformation and dispersal of sediment by buoyant coastal flows, Continental Shelf Research, 24, 927-949, 10.1016/j.csr.2004.02.006, 2004.

Gong, W., Lin, Z., Chen, Y., Chen, Z., Shen, J., and Zhang, H.: Effect of waves on the dispersal of the Pearl River plume in winter, Journal of Marine Systems, 186, 47-67, 10.1016/j.jmarsys.2018.05.003, 2018.

Hanebuth, T. J. J., Lantzsch, H., and Nizou, J.: Mud depocenters on continental shelves—appearance, initiation times, and growth dynamics, Geo-Marine Letters, 35, 487-503, 10.1007/s00367-015-0422-6, 2015.

Harff, J., Leipe, T., and Zhou, D.: Pearl River Estuary related sediments as response to Holocene climate change and anthropogenic impact (PECAI), Journal of Marine Systems, 82, S1-S2, 10.1016/j.jmarsys.2010.02.008, 2010.

Harris, C. K., Traykovski, P. A., and Geyer, W. R.: Flood dispersal and deposition by near-bed gravitational sediment flows and oceanographic transport: A numerical modeling study of the Eel River shelf, northern California, Journal of Geophysical Research: Oceans, 110, 10.1029/2004jc002727, 2005.

Harris, C. K., Sherwood, C. R., Signell, R. P., Bever, A. J., and Warner, J. C.: Sediment dispersal in the northwestern Adriatic Sea, Journal of Geophysical Research, 113, 10.1029/2006jc003868, 2008.

Hong, B., Liu, Z., Shen, J., Wu, H., Gong, W., Xu, H., and Wang, D.: Potential physical impacts of sea-level rise on the Pearl River Estuary, China, Journal of Marine Systems, 201, 103245, 10.1016/j.jmarsys.2019.103245, 2020.

Horner-Devine, A. R., Hetland, R. D., and MacDonald, D. G.: Mixing and Transport in Coastal River Plumes, Annual Review of Fluid Mechanics, 47, 569-594, 10.1146/annurev-fluid-010313-141408, 2015.

Hu, J., Li, S., and Geng, B.: Modeling the mass flux budgets of water and suspended sediments for the river network and estuary in the Pearl River Delta, China, Journal of Marine Systems, 88, 252-266, 10.1016/j.jmarsys.2011.05.002, 2011.

Huang, D., Du, J., Deng, B., and Zhang, J.: Distribution patterns of particle-reactive radionuclides in sediments off eastern Hainan Island, China: Implications for source and transport pathways, Continental Shelf Research, 57, 10-17, 10.1016/j.csr.2012.04.019, 2013.

Kirby, M. F., Devoy, B., Law, R. J., Ward, A., and Aldridge, J.: The use of a bioassay based approach to the hazard/risk assessment of cargo derived toxicity during shipping accidents: a case study--the MSC Napoli, Marine Pollution Bulletin, 56, 781-786, 10.1016/j.marpolbul.2008.01.006, 2008.

Krige, D. G.: A Statistical Approach to Some Basic Mine Valuation Problems on the Witwatersrand, Chemical, Metallurgical and Mining Society of South Africa, 1951.

Kuehl, S. A., Alexander, C. R., Blair, N. E., Harris, C. K., Marsaglia, K. M., Ogston, A. S., Orpin, A. R., Roering, J. J., Bever, A. J., Bilderback, E. L., Carter, L., Cerovski-Darriau, C., Childress, L. B., Reide Corbett, D., Hale, R. P., Leithold, E. L., Litchfield, N., Moriarty, J. M., Page, M. J., Pierce, L. E. R., Upton, P., and Walsh, J. P.: A source-to-sink perspective of the Waipaoa River margin, Earth-Science Reviews, 153, 301-334, 10.1016/j.earscirev.2015.10.001, 2016.

Kumar, N., Voulgaris, G., Warner, J. C., and Olabarrieta, M.: Implementation of the vortex force formalism in the coupled ocean-atmosphere-wave-sediment transport (COAWST) modeling system for inner shelf and surf zone applications, Ocean Modelling, 47, 65-95, 10.1016/j.ocemod.2012.01.003, 2012.

Lai, Z., Ma, R., Huang, M., Chen, C., Chen, Y., Xie, C., and Beardsley, R. C.: Downwelling wind, tides, and estuarine plume dynamics, Journal of Geophysical Research: Oceans, 121, 4245-4263, 10.1002/2015jc011475, 2016.

LaRowe, D. E., Arndt, S., Bradley, J. A., Estes, E. R., Hoarfrost, A., Lang, S. Q., Lloyd, K. G., Mahmoudi, N., Orsi, W. D., Shah Walter, S. R., Steen, A. D., and Zhao, R.: The fate of organic carbon in marine sediments - New insights from recent data and analysis, Earth-Science Reviews, 204, 103146, 10.1016/j.earscirev.2020.103146, 2020.

Li, Y., and Li, M.: Effects of winds on stratification and circulation in a partially mixed estuary, Journal of Geophysical Research, 116, 10.1029/2010jc006893, 2011.

Lin, S., Niu, J., Liu, G., Wei, X., and Cai, S.: Variations of suspended sediment transport caused by changes in shoreline and bathymetry in the Zhujiang (Pearl) River Estuary in the wet season, Acta Oceanologica Sinica, 41, 54-73, 10.1007/s13131-022-2017-1, 2022.

Lin, W., Feng, Y., Yu, K., Lan, W., Wang, Y., Mo, Z., Ning, Q., Feng, L., He, X., and Huang, Y.: Long-lived radionuclides in marine sediments from the Beibu Gulf, South China Sea: Spatial distribution, controlling factors, and proxy for transport pathway, Marine Geology, 424, 106157, 10.1016/j.margeo.2020.106157, 2020.

Liu, G., and Cai, S.: Modeling of suspended sediment by coupled wave-current model in the Zhujiang (Pearl) River Estuary, Acta Oceanologica Sinica, 38, 22-35, 10.1007/s13131-019-1455-3, 2019.

Liu, H., Ye, L., Zhou, W., and Wu, J.: Salt-wedge intrusion-retreat cycle induced sediment floc dynamics in bottom boundary layer (BBL) of a micro-tidal estuary, Marine Geology, 466, 107175, 10.1016/j.margeo.2023.107175, 2023.

Liu, Y., Gao, S., Wang, Y. P., Yang, Y., Long, J., Zhang, Y., and Wu, X.: Distal mud deposits associated with the Pearl River over the northwestern continental shelf of the South China Sea, Marine Geology, 347, 43-57, 10.1016/j.margeo.2013.10.012, 2014.

Liu, Z., Zhao, Y., Colin, C., Stattegger, K., Wiesner, M. G., Huh, C.-A., Zhang, Y., Li, X., Sompongchaiyakul, P., You, C.-F., Huang, C.-Y., Liu, J. T., Siringan, F. P., Le, K. P., Sathiamurthy, E., Hantoro, W. S., Liu, J., Tuo, S., Zhao, S., Zhou, S., He, Z., Wang, Y., Bunsomboonsakul, S., and Li, Y.: Source-to-sink transport processes of fluvial sediments in the South China Sea, Earth-Science Reviews, 153, 238-273, 10.1016/j.earscirev.2015.08.005, 2016.

Lu, X., Wang, Z., Guo, X., Gu, Y., Liang, W., and Liu, L.: Impacts of metal contamination and eutrophication on dinoflagellate cyst assemblages along the Guangdong coast of southern China, Marine Pollution Bulletin, 120, 239-249, 10.1016/j.marpolbul.2017.05.032, 2017.

Ma, Y., Friedrichs, C. T., Harris, C. K., and Wright, L. D.: Deposition by seasonal wave- and current-supported sediment gravity flows interacting with spatially varying bathymetry: Waiapu shelf, New Zealand, Marine Geology, 275, 199-211, https://doi.org/10.1016/j.margeo.2010.06.001, 2010.

Madsen, O. S.: Spectral Wave-Current Bottom Boundary Layer Flows, Coastal Engineering 1, 384-398, 1994.

Mao, Q., Shi, P., Yin, K., Gan, J., and Qi, Y.: Tides and tidal currents in the Pearl River Estuary, Continental Shelf Research, 24, 1797-1808, 10.1016/j.csr.2004.06.008, 2004.

McWilliams, J. C., Restrepo, J. M., and Lane, E. M.: An asymptotic theory for the interaction of waves and currents in coastal waters, Journal of Fluid Mechanics, 511, 135-178, 10.1017/s0022112004009358, 2004.

Meade, R. H.: Landward Transport of Bottom Sediments in Estuaries of the Atlantic Coastal Plain, Journal of Sedimentary Petrology, 39, 222-234, 1969.

Moriarty, J. M., Harris, C. K., Friedrichs, M. A. M., Fennel, K., and Xu, K.: Impact of Seabed Resuspension on Oxygen and Nitrogen Dynamics in the Northern Gulf of Mexico: A Numerical Modeling Study, Journal of Geophysical Research: Oceans, 123, 7237-7263, https://doi.org/10.1029/2018JC013950, 2018.

Ning, L., and Qian, Y.: Interdecadal change in extreme precipitation over South China and its mechanism, Advances in Atmospheric Sciences, 26, 109-118, 10.1007/s00376-009-0109-x, 2009.

Orlanski, I.: A simple boundary condition for unbounded hyperbolic flows, Journal of Computational Physics, 21, 251-269, 10.1016/0021-9991(76)90023-1, 1976.

Ralston, D. K., Geyer, W. R., and Warner, J. C.: Bathymetric controls on sediment transport in the Hudson River estuary: Lateral asymmetry and frontal trapping, Journal of Geophysical Research: Oceans, 117, 10.1029/2012jc008124, 2012.

Ralston, D. K., and Geyer, W. R.: Sediment Transport Time Scales and Trapping Efficiency in a Tidal River, Journal of Geophysical Research: Earth Surface, 122, 2042-2063, 10.1002/2017jf004337, 2017.

Raymond, W. H., and Kuo, H. L.: A radiation boundary condition for multi-dimensional flows, Quarterly Journal of the Royal Meteorological Society, 110, 535-551, 1984.

Repasch, M., Scheingross, J. S., Hovius, N., Lupker, M., Wittmann, H., Haghipour, N., Gröcke, D. R., Orfeo, O., Eglinton, T. I., and Sachse, D.: Fluvial organic carbon cycling regulated by sediment transit time and mineral protection, Nature Geoscience, 14, 842-848, 10.1038/s41561-021-00845-7, 2021.

Rong, Z., Hetland, R. D., Zhang, W., and Zhang, X.: Current–wave interaction in the Mississippi–Atchafalaya river plume on the Texas–Louisiana shelf, Ocean Modelling, 84, 67-83, 10.1016/j.ocemod.2014.09.008, 2014.

Shepard, F. P.: Nomenclature Based on Sand-silt-clay Ratios, Journal of Sedimentary Research, 24, 151-158, 1954.

Sherwood, C. R., Aretxabaleta, A. L., Harris, C. K., Rinehimer, J. P., Verney, R., and Ferré, B.: Cohesive and mixed sediment in the Regional Ocean Modeling System (ROMS v3.6) implemented in the Coupled Ocean–Atmosphere–Wave–Sediment Transport Modeling System (COAWST r1234), Geoscientific Model Development, 11, 1849-1871, 10.5194/gmd-11-1849-2018, 2018.

Shi, M., Chen, C., Xu, Q., Lin, H., Liu, G., Wang, H., Wang, F., and Yan, J.: The Role of Qiongzhou Strait in the Seasonal Variation of the South China Sea Circulation, Journal of Physical Oceanography, 32, 103-121, 2002.

Smagorinsky, J.: GENERAL CIRCULATION EXPERIMENTS WITH THE PRIMITIVE EQUATIONS, Monthly Weather Review, 91, 99-164, 10.1175/1520-0493(1963)091<0099:gcewtp>2.3.co;2, 1963.

Song, Y., and Haidvogel, D.: A Semi-implicit Ocean Circulation Model Using a Generalized Topography-Following Coordinate System, Journal of Computational Physics, 115, 228-244, https://doi.org/10.1006/jcph.1994.1189, 1994.

Ståhlberg, C., Bastviken, D., Svensson, B. H., and Rahm, L.: Mineralisation of organic matter in coastal sediments at different frequency and duration of resuspension, Estuarine, Coastal and Shelf Science, 70, 317-325, https://doi.org/10.1016/j.ecss.2006.06.022, 2006.

Su, J.: Overview of the South China Sea circulation and its influence on the coastal physical oceanography outside the Pearl River Estuary, Continental Shelf Research, 24, 1745-1760, 10.1016/j.csr.2004.06.005, 2004.

Turner, A., and Millward, G. E.: Suspended Particles: Their Role in Estuarine Biogeochemical Cycles, Estuarine, Coastal and Shelf Science, 55, 857-883, 10.1006/ecss.2002.1033, 2002.

van der Wegen, M., Dastgheib, A., Jaffe, B. E., and Roelvink, D.: Bed composition generation for morphodynamic modeling: case study of San Pablo Bay in California, USA, Ocean Dynamics, 61, 173-186, 10.1007/s10236-010-0314-2, 2010.

Walsh, J. P., and Nittrouer, C. A.: Understanding fine-grained river-sediment dispersal on continental margins, Marine Geology, 263, 34-45, 10.1016/j.margeo.2009.03.016, 2009.

Wang, S., Zhang, N., Chen, H., Li, L., and Yan, W.: The surface sediment types and their rare earth element characteristics from the continental shelf of the northern south China sea, Continental Shelf Research, 88, 185-202, 10.1016/j.csr.2014.08.005, 2014.

Wang, S., Wu, S., Yan, W., Huang, W., Miao, L., Lu, J., Chen, Z., and Liu, F.: Rare metal elements in surface sediment from five bays on the northeastern coast of the South China Sea, Environmental Earth Sciences, 74, 4961-4971, 10.1007/s12665-015-4504-6, 2015.

Wang, S., Li, J., Wu, S., Yan, W., Huang, W., Miao, L., and Chen, Z.: The distribution characteristics of rare metal elements in surface sediments from four coastal bays on the northwestern South China Sea, Estuarine, Coastal and Shelf Science, 169, 106-118, 10.1016/j.ecss.2015.12.001, 2016.

Wang, Y., Wang, Y., Wan, X., Huang, C., Wang, R., Liu, X., Yi, J., and Zhang, Y.: Influence of the Hanjiang River's Inlet Sediment Decrease on Modern Sedimentation in the Underwater Delta, Applied Sciences, 13, 8039, 10.3390/app13148039, 2023.

Warner, J. C., Sherwood, C. R., Arango, H. G., and Signell, R. P.: Performance of four turbulence closure models implemented using a generic length scale method, Ocean Modelling, 8, 81-113, 10.1016/j.ocemod.2003.12.003, 2005.

Warner, J. C., Sherwood, C. R., Signell, R. P., Harris, C. K., and Arango, H. G.: Development of a three-dimensional, regional, coupled wave, current, and sediment-transport model, Computers & Geosciences, 34, 1284-1306, 10.1016/j.cageo.2008.02.012, 2008.

Warner, J. C., Armstrong, B., He, R., and Zambon, J. B.: Development of a Coupled Ocean–Atmosphere–Wave–Sediment Transport (COAWST) Modeling System, Ocean Modelling, 35, 230-244, 10.1016/j.ocemod.2010.07.010, 2010.

Warner, J. C., Schwab, W. C., List, J. H., Safak, I., Liste, M., and Baldwin, W.: Inner-shelf ocean dynamics and seafloor morphologic changes during Hurricane Sandy, Continental Shelf Research, 138, 1-18, 10.1016/j.csr.2017.02.003, 2017.

Wright, L. D., and Coleman, J. M.: Variations in Morphology of Major River Deltas as Functions of Ocean Wave and River Discharge Regimes, AAPG Bulletin, 57, 370-398, 1973.

Wright, L. D., and Nittrouer, C. A.: Dispersal of river sediments in coastal seas: Six contrasting cases, Estuaries, 18, 494-508, 10.2307/1352367, 1995.

Wu, C., Xing, W., Jie, R., Yun, B., Zhigang, H., Yiaping, L., Heyin, S., and Wenyan, Z.: Morphodynamics of the rock-bound outlets of the Pearl River estuary, South China — A preliminary study, Journal of Marine Systems, 82, S17-S27, 10.1016/j.jmarsys.2010.02.002, 2010.

Wu, Z., Milliman, J. D., Zhao, D., Zhou, J., and Yao, C.: Recent geomorphic change in LingDing Bay, China, in response to economic and urban growth on the Pearl River Delta, Southern China, Global and Planetary Change, 123, 1-12, 10.1016/j.gloplacha.2014.10.009, 2014.

Wu, Z., Milliman, J. D., Zhao, D., Cao, Z., Zhou, J., and Zhou, C.: Geomorphologic changes in the lower Pearl River Delta, 1850–2015, largely due to human activity, Geomorphology, 314, 42-54, 10.1016/j.geomorph.2018.05.001, 2018.

Wu, Z. Y., Saito, Y., Zhao, D. N., Zhou, J. Q., Cao, Z. Y., Li, S. J., Shang, J. H., and Liang, Y. Y.: Impact of human activities on subaqueous topographic change in Lingding Bay of the Pearl River estuary, China, during 1955-2013, Scientific Reports, 6, 37742, 10.1038/srep37742, 2016.

Xia, X. M., Li, Y., Yang, H., Wu, C. Y., Sing, T. H., and Pong, H. K.: Observations on the size and settling velocity distributions of suspended sediment in the Pearl River Estuary, China, Continental Shelf Research, 24, 1809-1826, 10.1016/j.csr.2004.06.009, 2004.

Xue, Z., He, R., Liu, J. P., and Warner, J. C.: Modeling transport and deposition of the Mekong River sediment, Continental Shelf Research, 37, 66-78, 10.1016/j.csr.2012.02.010, 2012.

Yang, B., Liu, S.-M., and Zhang, G.-L.: Geochemical characteristics of phosphorus in surface sediments from the continental shelf region of the northern South China Sea, Marine Chemistry, 198, 44-55, 10.1016/j.marchem.2017.11.001, 2018.

Yang, Y., Guan, W., Deleersnijder, E., and He, Z.: Hydrodynamic and sediment transport modelling in the Pearl River Estuary and adjacent Chinese coastal zone during Typhoon Mangkhut, Continental Shelf Research, 233, 104645, 10.1016/j.csr.2022.104645, 2022.

Young, I. R., Zieger, S., and Babanin, A. V.: Global trends in wind speed and wave height, Science, 332, 451-455, 10.1126/science.1197219, 2011.

Zhang, G., Cheng, W., Chen, L., Zhang, H., and Gong, W.: Transport of riverine sediment from different outlets in the Pearl River Estuary during the wet season, Marine Geology, 415, 105957, 10.1016/j.margeo.2019.06.002, 2019.

Zhang, G., Chen, Y., Cheng, W., Zhang, H., and Gong, W.: Wave Effects on Sediment Transport and Entrapment in a Channel-Shoal Estuary: The Pearl River Estuary in the Dry Winter Season, Journal of Geophysical Research: Oceans, 126, 10.1029/2020jc016905, 2021.

Zhang, J., Jiang, Q., Jeng, D., Zhang, C., Chen, X., and Wang, L.: Experimental Study on Mechanism of Wave-Induced Liquefaction of Sand-Clay Seabed, Journal of Marine Science and Engineering, 8, 66, 10.3390/jmse8020066, 2020.

Zhang, W., Wei, X., Zheng, J., Zhu, Y., and Zhang, Y.: Estimating suspended sediment loads in the Pearl River Delta region using sediment rating curves, Continental Shelf Research, 38, 35-46, 10.1016/j.csr.2012.02.017, 2012.

Zhang, W., Zheng, J., Ji, X., Hoitink, A. J. F., van der Vegt, M., and Zhu, Y.: Surficial sediment distribution and the associated net sediment transport pattern retain-->in the Pearl River Estuary, South China, Continental Shelf Research, 61-62, 41-51, 10.1016/j.csr.2013.04.011, 2013.

Zhong, Y., Chen, Z., Li, L., Liu, J., Li, G., Zheng, X., Wang, S., and Mo, A.: Bottom water hydrodynamic provinces and transport patterns of the northern South China Sea: Evidence from grain size of the terrigenous sediments, Continental Shelf Research, 140, 11-26, 10.1016/j.csr.2017.01.023, 2017.

Zhu, L., Gong, W., Zhang, H., Huang, W., and Zhang, R.: Numerical study of sediment transport time scales in an ebb-dominated waterway, Journal of Hydrology, 591, 125299, 10.1016/j.jhydrol.2020.125299, 2020.

Zhu, L., Zhang, H., Guo, L., Huang, W., and Gong, W.: Estimation of riverine sediment fate and transport timescales in a wide estuary with multiple sources, Journal of Marine Systems, 214, 103488, 10.1016/j.jmarsys.2020.103488, 2021.

Zong, X., Cheng, X., Zhang, S., Lian, Q., Deng, F., and Chen, Z.: Tidal effects on dynamics and freshwater transport of a medium-scale river plume with multiple outlets, Ocean Modelling, 188, 102338, https://doi.org/10.1016/j.ocemod.2024.102338, 2024.